Exploratory X-Ray Monitoring of Luminous Radio-quiet Quasars at High Redshift: Extended Time-series Analyses and Stacked Imaging Spectroscopy

Marcus O. Thomas[1] , Ohad Shemmer[1] , W. N. Brandt[2,3,4] , Maurizio Paolillo[5,6,7] , Shai Kaspi[8] , Cristian Vignali[9,10] ,
Paulina Lira[11] , and Donald P. Schneider[2,3]

[1] Department of Physics, University of North Texas, Denton, TX 76203, USA; MarcusThomas@my.unt.edu
[2] Department of Astronomy and Astrophysics, 525 Davey Lab, The Pennsylvania State University, University Park, PA 16802, USA
[3] Institute for Gravitation and the Cosmos, The Pennsylvania State University, University Park, PA 16802, USA
[4] Department of Physics, 104 Davey Lab, The Pennsylvania State University, University Park, PA 16802, USA
[5] Dipartimento di Scienze Fisiche, Università Federico II di Napoli, via Cintia 6, I-80126 Napoli, Italy
[6] Agenzia Spaziale Italiana—Science Data Center, Via del Politecnico snc, I-00133 Roma, Italy
[7] INFN—Unità di Napoli, via Cintia 9, I-80126, Napoli, Italy
[8] School of Physics & Astronomy and the Wise Observatory, Tel Aviv University, Tel Aviv 69978, Israel
[9] Dipartimento di Fisica e Astronomia "Augusto Righi," Università degli Studi di Bologna, Via Gobetti 93/2, I-40129 Bologna, Italy
[10] INAF—Osservatorio di Astrofisica e Scienza dello Spazio di Bologna, Via Gobetti 93/3, I-40129 Bologna, Italy
[11] Departamento de Astronomia, Universidad de Chile, Camino del Observatorio 1515, Santiago, Chile

Abstract

We present three new Chandra X-ray epochs along with new ground-based optical–UV observations as the third installment in a time-series analysis of four high-redshift ($z \approx 4.1$–4.4) radio-quiet quasars. In total, we present nine epochs for these sources with rest-frame temporal baselines of ∼1300–2000 days. We utilize the X-ray data to determine basic variability properties, as well as produce mean spectra and stacked images based on effective exposure times of ∼40–70 ks per source. We perform time-series analyses in the soft and hard bands, separately, and compare variability properties to those of sources at lower redshifts and luminosities. The magnitude of X-ray variability of our sources remains consistent with or lower than that of similar sources at lower redshifts, in agreement with the variability–luminosity anticorrelation. The mean power-law photon indices in the stacked Chandra spectra of our sources are consistent with the values measured from their archival XMM-Newton spectra separated by about 3 yr in the rest frame. Along with the X-ray observations, we provide near-simultaneous optical monitoring of the sources in the optical–UV regime. The overall variability in the optical-to-X-ray spectral slope is consistent with sources at lower redshifts, and the optical–UV observations display mild variability on monthly timescales.

Unified Astronomy Thesaurus concepts: Active galaxies (17); Quasars (1319); Radio quiet quasars (1354); X-ray active galactic nuclei (2035)

1. Introduction

Long-term variability studies of distant quasars are important for understanding the evolution of active galactic nuclei (AGNs) over cosmic time (e.g., Kaspi et al. 2007; Trevese et al. 2008; MacLeod et al. 2012; Yang et al. 2016; Timlin et al. 2020). X-rays, in particular, are critical to study as they generally have stronger variations on shorter timescales than those of lower energy bands (see, e.g., Mushotzky et al. 1993). X-ray variability studies can provide powerful probes of quasars' inner ∼10 gravitational radii and important information on the structure of the central engine (see, e.g., Lawrence & Papadakis 1993; Lanzuisi et al. 2014; Ricci et al. 2020), including the mass and accretion rate of the supermassive black hole (see, e.g., McHardy et al. 2006; Kelly et al. 2013; La Franca et al. 2014; Paolillo et al. 2017, hereafter P17).

Nearby quasars show an anticorrelation between X-ray variability and luminosity (e.g., Lawrence & Papadakis 1993). However, their high-redshift counterparts are poorly sampled (see, e.g., Nanni et al. 2017; Vito et al. 2019; Wang et al. 2021, for recent reviews), and this trend was not so clear for sources at $z \gtrsim 1$ (see, e.g., Vagnetti et al. 2011; Gibson & Brandt 2012; Yang et al. 2016), including the peak of quasar activity (e.g., Richards et al. 2006). Quite a few high-redshift, and therefore luminous, AGNs have displayed significant X-ray variability on timescales of months to years (see, e.g., Paolillo et al. 2004;

Shemmer et al. 2014, hereafter Paper I; Vagnetti et al. 2016). Several studies have suggested that the observed variability evolves with redshift (e.g., Almaini et al. 2000; Manners et al. 2002; Paolillo et al. 2004; Papadakis et al. 2008), which is difficult to reconcile with the relative consistency of the basic X-ray properties of AGNs up to $z \sim 7$ (e.g., Shemmer et al. 2005, 2006a; Vignali et al. 2005; Steffen et al. 2006; Just et al. 2007; Vito et al. 2019). Other works suggest, instead, a lack of evolution with redshift (e.g., Lanzuisi et al. 2014; P17).

In light of this discrepancy, we began an X-ray monitoring survey using the Chandra X-ray Observatory (hereafter Chandra; Weisskopf et al. 2000) of four representative radio-quiet quasars (RQQs[12]) with redshifts between 4.10 and 4.35 (hereafter "Chandra sources"; see Paper I). The sources, Q0000−263, BR 0351−1034, PSS 0926+3055, and PSS 1326+0743, were selected out of the sample of Shemmer et al. (2005) as having the highest accessible redshifts for economical Chandra observations and having at least two archival X-ray epochs.

Paper I presented the variability information based on four X-ray epochs, two of which were archival, which was

---

compared to a sample of similarly luminous quasars at considerably lower redshifts ($1.33 < z < 2.74$), observed with the Neil Gehrels Swift Observatory (Gehrels et al. 2004; hereafter "Swift sources"), as well as nearby quasars (i.e., $0 \lesssim z \lesssim 0.3$) from Fiore et al. (1998). The initial findings revealed that the Chandra sources exhibited X-ray variability similar to far less luminous nearby AGNs, which appeared at odds with the anticorrelation between X-ray variability and luminosity observed in the nearby universe. However, the higher-redshift Chandra sources exhibited, on average, a smaller variability amplitude than the Swift sources, indicating that X-ray variability does not necessarily increase with redshift. Further, three of the four Chandra sources were considered X-ray variable following a χ^2 test on their light curves.

Shemmer et al. (2017, hereafter Paper II) strengthened Paper I's conclusion that X-ray variability does not depend on redshift and the addition of two Chandra epochs for each of our Chandra sources reduced the number of variable objects to one. When considering only the Chandra observations of the Chandra sources, no significant X-ray variability was detected in any of these sources. Paper II also presented a comparison with the "bright-R" sample ($0.42 \leqslant z \leqslant 3.70$; P17) of 94 quasars from the 7 Ms Chandra Deep Field-South survey (CDF-S; Luo et al. 2017), spanning over 17 yr in the observed frame. The comparison of the Chandra, Swift, and the less luminous CDF-S sources revealed the trend of increasing X-ray variability amplitude with decreasing luminosity and offered no evidence of X-ray variability increasing with redshift.

In this paper, we present three additional Chandra epochs for the Chandra sources (nine X-ray epochs in total), which allow us to extend our time-series analysis and produce tighter constraints on the X-ray properties of these sources. Using these new data, we are now able to present mean imaging spectroscopy and deep X-ray imaging spanning 3.5 yr in the rest frame for PSS 0926+3055 and PSS 1326+0743 and nearly 2 yr in the rest frame for Q0000−263 and BR 0351−1034. We also perform all prior and new data reduction and variability analysis on the Chandra data using a more reliable method for flux calculation, extend the analysis into the Chandra hard band (2–8 keV), and perform Monte Carlo simulations to strengthen our variability classifications.

This paper is organized as follows: Section 2 presents the data obtained from the three new epochs, as well as our means of data reduction and analysis. Section 3 details the need for and implementation of light-curve simulations for each source, extends our prior time-series analysis, and presents stacked Chandra images and mean spectra. This section also presents our ground-based optical observations of these objects taken close in time to the Chandra observations. Section 4 provides a summary of our findings. Appendix A describes the effects of contamination buildup on the Chandra detector pertaining to our analysis, and Appendix B reports the spectral properties of previously published epochs reprocessed with the new methods used in this work. Luminosity distances were computed using the standard cosmological model ($\Omega_\Lambda = 0.7$, $\Omega_M = 0.3$, and $H_0 = 70$ km s^{-1} Mpc^{-1}; e.g., Spergel et al. 2007).

2. X-Ray Observations and Data Reduction

Paper II reported on six epochs from each of the four sources gathered by Chandra between 2003 and 2017, along with observations from XMM-Newton (Jansen et al. 2001) from

2002 and 2004 and ROSAT (Aschenbach et al. 1981) observations from 1991 and 1992. Three new epochs are provided here, per source, all obtained with Chandra Advanced CCD Imaging Spectrometer (ACIS; Garmire et al. 2003) snapshots during Cycles 19, 20, and 21. The Chandra observation log is presented in Table 1. The data reduction methods used in Papers I and II have been shown to potentially produce significant bias in low-count X-ray observations due to older and out-of-date instrument calibrations,[13] and they have therefore been retired in favor of new methods described below. All previously reported Chandra observations have been reduced using these new tools, which consider regularly updated quantum efficiency (QE) degradation and charge transfer inefficiency (CTI) models, as described in Appendix A, and their spectral properties are reported in Appendix B.

Source counts and fluxes were extracted using Chandra Interactive Analysis of Observations (CIAO)[14] v4.12 tools and CIAO Calibration Database (CALDB)[15] v4.9.3. All Chandra observations were reprocessed with the *chandra_repro* script to apply the latest instrument calibrations. In each case, the source-count results were consistent with those previously reported.

Papers I and II reported on the ultrasoft (0.3–0.5 keV) band, but given the lack of detectable counts (amounting to a formal upper limit of three counts) from each object in the new epochs, this band is omitted in this work. Observed-frame counts in the X-ray soft (0.5–2 keV), hard (2–8 keV), and full (0.5–8 keV) bands were measured using `wavdetect` (Freeman et al. 2002), utilizing wavelet transforms with a false-positive threshold of 10^{-3}, as the X-ray coordinates were known a priori and were confirmed by visual inspection of the images. For the new epochs, Table 2 reports the counts in each band, the soft-band count rate, effective power-law photon index (Γ_{eff}, 0.5–8.0 keV), band ratio calculated with `Bayesian Estimation of Hardness Ratios` (BEHR; Park et al. 2006), and Galactic-absorption-corrected flux density at rest-frame 2 keV. Effective photon indices and their 90% uncertainties were estimated using spectral modeling in `Sherpa` (Freeman et al. 2001). The flux density at rest-frame 2 keV measurement methods are described below.

Soft- and hard-band unabsorbed source fluxes were obtained using two methods. Previously, Papers I and II reported fluxes obtained using Chandra PIMMS,[16] which is purposed for observation planning and estimates a model-based flux with user-provided parameters. However, while popular, this method has pitfalls when used to calculate fluxes for observed data. The tool is intended to function as a proposal-planning toolkit, and the calibrations applied to the latest Chandra Cycles are *predictions* rather than based on up-to-date instrument conditions. While Chandra PIMMS considers these calibration factors, the models are predictions of what the instrument conditions will be at the beginning of the next observation cycle, ∼18 months in the future, and are not updated beyond the initial prediction.

According to the Chandra X-ray Center (CXC), due to the loss of sensitivity to lower-energy photons, as well as the loss of effective area due to contamination buildup, the most reliable way to calculate fluxes is to use the CIAO thread *srcflux*

---

[13] See https://cxc.harvard.edu/ciao/why/pimms.html.
[14] http://cxc.cfa.harvard.edu/ciao/
[15] http://cxc.harvard.edu/ciao/ahelp/caldb.html
[16] https://cxc.harvard.edu/toolkit/pimms.jsp

Table 1
Log of New Chandra Observations

Quasar	α (J2000.0)	δ (J2000.0)	z	Galactic N_H[a] $(10^{20}$ cm$^{-2})$	Cycle	Obs. Date	Obs. ID	Exp. Time[b] (ks)
Q0000−263	00 03 22.9	−26 03 16.8	4.10	1.67	19	2018 Sep 1	20606	9.83
...	...	...		...	20	2019 Aug 13	20607[c]	9.85
...	...	...		...	21	2020 Aug 15	20608	9.94
BR 0351−1034	03 53 46.9	−10 25 19.0	4.35	4.08	19	2018 Oct 24	20609	9.94
...	...	...		...	20	2019 Nov 1	20610[c]	9.83
...	...	...		...	21	2020 Oct 28	20611	9.26
PSS 0926+3055	09 26 36.3	+30 55 05.0	4.19	1.89	19	2018 Mar 9	20600	4.99
...	...	...		...	20	2019 Jan 8	20601[c]	4.89
...	...	...		...	21	2020 Jan 25	20602[c]	4.89
PSS 1326+0743	13 26 11.9	+07 43 58.4	4.17	2.01	19	2018 Apr 30	20603	4.90
...	...	...		...	20	2019 Apr 30	20604[c]	5.05
...	...	...		...	21	2020 Mar 26	20605[c]	4.99

Notes.
[a] Obtained from Dickey & Lockman (1990) using the N_H tool at http://heasarc.gsfc.nasa.gov/cgi-bin/Tools/w3nh/w3nh.pl.
[b] Exposure time was adjusted to account for detector dead time.
[c] Reprocessed by the CXC as part of the Repro-V Campaign https://cxc.cfa.harvard.edu/cda/repro5.html.

on observed data. The *srcflux* thread is a wrapper that calculates both the model-independent position-based flux using the thread *eff2evt* and a power law with photoelectric absorption model-based flux with *modelflux*, given user-provided photon indices and N_H parameters. Using this thread, we extracted unabsorbed source fluxes in the soft and hard bands, accounting for up-to-date CCD effective-area loss, CTI, and point-spread function (PSF) contribution.

When specifying an energy range for *srcflux* to integrate over, the user must provide a monochromatic energy to properly weight the detector response area based on the PSF contribution. We used the monochromatic energy 1.35 and 3.4 keV in the soft and hard band, respectively, based on the absorption edges in the response near the band boundaries. With the loss of effective area over the range of this monitoring program, the selection of a single monochromatic energy over all epochs can cause significant offsets in flux.[17] Further, the user-provided photon index for each object, in this case, was the photon index of its mean spectrum over all epochs (see Section 3.4). Given that our analysis is contingent on the behavior of the sources at each individual epoch, more care should be taken when modeling the independent observations.

In order to find the most accurate model-based flux measurement, in addition to the *srcflux* estimates, the source spectrum of each Chandra observation was extracted from the level-2 event file with the thread *specextract*. The spectra were fit in Sherpa v14.3 using the XSPEC (Arnaud 1996) xspowerlaw single power-law and xsphabs Galactic-absorption models, along with a free normalization parameter. The xsphabs Galactic-absorption column density parameter for each source was frozen to the values in Table 1. The fits were made using the *cstat* statistic over the 0.5–8.0 keV energy range, with the data grouped into a minimum of one count per energy bin (e.g., Kaastra 2017; also, see Section 3.1.1 on χ^2 statistics in this low-count regime). Typically, it is recommended that the background spectrum be modeled along with the source spectrum when using the Cash statistic (Cash 1979). However, all of our observations are on-axis, and background counts in the 2″ source regions are negligible (i.e., $\langle N_{BG} \rangle \ll 1$).

Once the best-fit model was determined, all parameters were frozen and the "convolution" model component xscflux was applied to the power-law model component to calculate the unabsorbed energy flux to 90% confidence. The rest-frame unabsorbed 2 keV flux densities were estimated by extrapolating Γ_{eff} and the respective soft-band flux using the PIMMS command-line tool v4.11b (Mukai 1993).

To summarize, the soft- and hard-band source fluxes were estimated in two ways: (1) *srcflux*, with a single mean photon index for all epochs, per source, and a constant monochromatic energy for the soft and hard band, respectively; and (2) by manual spectral fitting in Sherpa without assumed photon indices. Both of these methods avoid the potential offset caused by Chandra PIMMS predictions. Individual spectral modeling was favored over *srcflux* in all proceeding analyses in light of overall smaller uncertainties. However, we retain results from both methods for the following reasons: (1) to observe whether the selection of a single $\langle \Gamma \rangle$ and monochromatic flux produced a significant effect on our sources' flux estimates, (2) for comparison with the previously published results, and (3) for reference about the aforementioned parameter-selection effects on both methods of calculating flux in low-count observations for future studies. The results from both methods are reported in Table 3, along with those of the archival XMM-Newton and ROSAT observations.

3. Results and Discussion

The soft- and hard-band fluxes for all nine epochs of the Chandra sources are reported in Table 3, and the corresponding light curves are presented in Figure 1. These light curves constitute the most detailed X-ray light curves for RQQs at $z > 4$ and span the longest temporal baseline currently available (see, e.g., Yang et al. 2016). As can be seen in the light curves, the resultant source fluxes using both methods are consistent within the 90% uncertainties, albeit with differences in the size of the uncertainties. On average, the uncertainties calculated with *srcflux* are ~33% larger than those obtained using Sherpa in the soft band, and > 80% larger in the hard band, potentially due to the selection of $\langle \Gamma \rangle$ and the estimated PSF contribution from the assumed monochromatic flux (see Section 2). Given the smaller

---

[17] https://cxc.harvard.edu/ciao/why/monochromatic_energy.html

Table 2
Basic X-Ray Measurements

Quasar	Cycle	Counts[a]			Band Ratio[b]	$\Gamma_{\rm eff}$[c]	Count Rate[d]	$f_{\rm 2\,keV}$[c]
		0.5–2 keV	2–8 keV	0.5–8 keV				
Q0000−263	19	$27.7^{+6.3}_{-5.2}$	$8.6^{+4.1}_{-2.9}$	$38.2^{+7.2}_{-6.2}$	$0.30^{+0.27}_{-0.05}$	$2.5^{+0.7}_{-0.6}$	$2.8^{+0.6}_{-0.5}$	2.85
	20	$19.7^{+5.5}_{-4.4}$	$6.8^{+3.7}_{-2.5}$	$26.5^{+6.2}_{-5.1}$	$0.37^{+0.40}_{-0.06}$	$1.8^{+0.8}_{-0.7}$	$2.0^{+0.6}_{-0.4}$	0.97
	21	$23.5^{+5.9}_{-4.8}$	$18.8^{+5.4}_{-4.3}$	$42.2^{+7.6}_{-6.5}$	$0.78^{+0.43}_{-0.12}$	2.0 ± 0.5	$2.4^{+0.6}_{-0.5}$	2.29
BR 0351−1034	19	$14.8^{+4.9}_{-3.8}$	$3.9^{+3.2}_{-1.9}$	$18.6^{+5.4}_{-4.3}$	$0.23^{+0.47}_{-0.03}$	1.9 ± 1.0	$1.5^{+0.5}_{-0.4}$	0.99
	20	$8.4^{+4.0}_{-2.8}$	$9.8^{+4.2}_{-3.1}$	$18.2^{+5.4}_{-4.2}$	$1.19^{+1.76}_{-0.22}$	1.4 ± 0.8	$0.9^{+0.4}_{-0.3}$	0.48
	21	$7.9^{+3.9}_{-2.7}$	$5.0^{+3.4}_{-2.1}$	$12.8^{+4.7}_{-3.5}$	$0.56^{+1.35}_{-0.18}$	$2.4^{+1.3}_{-1.1}$	$0.8^{+0.4}_{-0.3}$	0.78
PSS 0926+3055	19	$8.9^{+4.1}_{-2.9}$	$8.9^{+4.1}_{-2.9}$	$18.8^{+5.4}_{-4.3}$	$0.95^{+1.31}_{-0.18}$	$1.5^{+1.1}_{-1.1}$	$1.8^{+0.8}_{-0.6}$	0.67
	20	$25.8^{+5.7}_{-4.6}$	$10.8^{+4.4}_{-3.2}$	$37.5^{+7.1}_{-6.0}$	$0.41^{+0.32}_{-0.06}$	2.1 ± 0.6	$5.5^{+1.3}_{-1.1}$	4.28
	21	$16.5^{+5.2}_{-4.0}$	$12.6^{+4.7}_{-3.5}$	$30.1^{+6.6}_{-5.5}$	$0.74^{+0.55}_{-0.13}$	1.4 ± 0.8	$3.4^{+1.0}_{-0.8}$	1.16
PSS 1326+0743	19	$18.6^{+5.4}_{-4.3}$	$4.9^{+3.4}_{-2.1}$	$28.3^{+6.4}_{-5.3}$	$0.23^{+0.37}_{-0.03}$	$1.7^{+0.6}_{-0.7}$	$3.8^{+1.1}_{-0.9}$	1.46
	20	$21.7^{+5.7}_{-4.6}$	$20.7^{+5.6}_{-4.5}$	$42.3^{+7.6}_{-6.5}$	$0.94^{+0.56}_{-0.14}$	1.6 ± 0.5	$4.3^{+1.1}_{-0.9}$	2.14
	21	$15.8^{+5.1}_{-3.9}$	$9.8^{+4.2}_{-3.1}$	$25.5^{+6.1}_{-5.0}$	$0.59^{+0.59}_{-0.10}$	1.8 ± 0.8	$3.2^{+1.0}_{-0.8}$	2.21

Notes. See Appendix B for updated measurements, using the new reduction methods, from epochs reported in Papers I and II.
[a] The 1σ level count errors were computed using Tables 1 and 2 of Gehrels (1986) with Poisson statistics. Note that 1σ corresponds to ~84% confidence in the Poisson limit. Counts at energies below ~0.5 keV have suffered significant QE losses and were omitted from this table owing to an upper limit of three counts per source per cycle (see Appendix A).
[b] Ratio of hard- to soft-band counts. To avoid the failure of the standard approximate-variance formula at small counts, band ratio and its 1σ level upper and lower limits were calculated using the software `Bayesian Estimation of Hardness Ratios` (BEHR; Park et al. 2006).
[c] Effective photon indices (0.5–8.0 keV; 90% confidence) were estimated by spectral modeling in `Sherpa`. See Section 2 for details on the assumed model. Galactic-absorption-corrected flux densities at rest-frame 2 keV in units of 10^{-31} erg cm^{-2} s^{-1} Hz^{-1} were estimated with the `PIMMS` command-line tool v4.11b (Mukai 1993) by extrapolating the respective soft-band flux (see Table 3) and $\Gamma_{\rm eff}$.
[d] Count rate computed in the soft band (observed-frame 0.5–2 keV) in units of 10^{-3} counts s^{-1}.

uncertainty ranges in the `Sherpa` fluxes, all following analyses are performed on these data rather than the *srcflux* measurements.

3.1. Time-Series Analysis and Simulations

Following the prescriptions of Papers I and II, we applied a χ^2 test to a source's light curve. In this work, we extend the test to the source's hard-band light curve, as well as at their effective photon indices ($\Gamma_{\rm eff}$). This test allows us to qualitatively determine whether a source is variable or not to a confidence of 90%, as well as make meaningful comparisons to lower-redshift objects that emit at similar rest-frame energies. The null hypothesis in the test is that the flux (or photon index) in each epoch is consistent, within the uncertainties, with that of the mean flux (or photon index) of the object over the entire light curve.

The χ^2 test is defined as

$$\chi^2 = \frac{1}{N_{\rm obs} - 1} \sum_{i=1}^{N_{\rm obs}} \frac{(f_i - \langle f \rangle)^2}{\sigma_i^2}, \qquad (1)$$

where f_i is the flux (or $\Gamma_{\rm eff,i}$), and σ_i its error, for the ith observation, $N_{\rm obs}$ is the number of epochs, and $\langle f \rangle$ is the mean flux of the light curve (or $\langle \Gamma_{\rm eff} \rangle$). The low-count nature of our data tends to produce asymmetric uncertainty bounds. In these cases, σ_i is the mean of the upper and lower uncertainty magnitudes. In order to consider effects of observatory-dependent flux calibrations, we repeated the χ^2 test for each source using only observations taken with Chandra for the soft band. For hard-band analysis, only Chandra epochs were considered.

3.1.1. χ^2 Tests in the Low-count Regime

It is well known that in the low-count regime the arrival of X-ray events differs significantly from a Gaussian distribution, and Poisson statistics must be considered. However, there has been debate as to the minimum number of counts per bin for the discrepancy in statistics to be negligible. While Poisson statistics approaches a Gaussian approximation at higher event rates, the statistical bias is evident in our sample, where, in several cases, fewer than 10 counts per band, per source, have been detected. Additionally, the asymmetric error approximations on our flux measurements function as upper and lower limits that are larger than those approximated from a normal distribution. This discrepancy can produce an overestimated χ^2 statistic when assuming Gaussian uncertainties (for detailed reviews on this statistical bias, see, e.g., Cash 1979; Nousek & Shue 1989; Mighell 1999).

In order to negate the potential bias and establish a reliable baseline on which to base our variability classification, we performed Monte Carlo simulations of our sources' light curves, similar to those performed in Paolillo et al. (2004). For each source, we simulated 1000 soft- and hard-band light curves with the assumption of nonvariability over all epochs for all observatories, and once again for only Chandra epochs.[18] Each simulated light curve was constructed by extracting $N_{\rm obs}$ random values from a Poisson distribution centered on the mean unabsorbed flux of the respective source. Then, the uncertainty for each epoch in the new light curve was calculated based on the uncertainty in the observation it represented. For example, if a source's second epoch had an uncertainty (σ_i) of 25% of its flux, a 25% uncertainty was applied to the second simulated observation in the light curve.

---

[18] Extending beyond 10^3 simulated light curves does not produce a significant increase in the precision or accuracy of the simulated statistics.

Table 3
Long-term X-Ray Light-curve Data

Quasar	JD	Flux (10^{-15} erg cm^{-2} s^{-1})				Observatory	Reference
		$f_{0.5-2\,\mathrm{keV}}$[a]		$f_{2-8\,\mathrm{keV}}$[a]			
Q0000−263	2,448,588.5	22 ± 3	⋯	⋯	⋯	ROSAT	1, 2, 3
	2,452,450.5	13 ± 1	⋯	⋯	⋯	XMM-Newton	4, 5, 6
	2,455,802.5	27^{+6}_{-5}	27^{+6}_{-6}	25^{+5}_{-5}	28^{+14}_{-6}	Chandra	7
	2,456,173.5	23^{+5}_{-4}	23^{+6}_{-6}	32^{+7}_{-6}	36^{+16}_{-6}	Chandra	7
	2,456,540.5	18^{+5}_{-4}	18^{+5}_{-6}	21^{+6}_{-5}	23^{+9}_{-6}	Chandra	8
	2,456,917.0	25^{+6}_{-5}	27^{+8}_{-8}	30^{+7}_{-6}	24^{+14}_{-8}	Chandra	8
	2,458,362.5	23^{+7}_{-6}	28^{+10}_{-10}	17^{+5}_{-4}	20^{+13}_{-10}	Chandra	9
	2,458,708.5	16^{+6}_{-5}	21^{+9}_{-9}	24^{+9}_{-7}	14^{+11}_{-9}	Chandra	9
	2,459,076.5	30^{+8}_{-7}	28^{+11}_{-11}	30^{+8}_{-7}	38^{+17}_{-11}	Chandra	9
	Mean Flux	22 ± 2	23 ± 2	26 ± 2	26 ± 3	⋯	
BR 0351−1034	2,448,647.5	15 ± 6	⋯	⋯	⋯	ROSAT	2, 3
	2,453,035.5	12 ± 2	⋯	⋯	⋯	XMM-Newton	5, 6, 10
	2,455,827.5	6^{+3}_{-2}	6^{+4}_{-3}	8^{+4}_{-3}	6^{+8}_{-3}	Chandra	7
	2,455,862.5	4^{+2}_{-2}	5^{+3}_{-2}	9^{+5}_{-4}	7^{+9}_{-2}	Chandra	7
	2,456,491.5	12^{+4}_{-4}	12^{+5}_{-4}	10^{+4}_{-3}	12^{+10}_{-4}	Chandra	8
	2,456,987.5	9^{+3}_{-3}	10^{+5}_{-4}	33^{+12}_{-10}	20^{+12}_{-4}	Chandra	8
	2,458,415.5	14^{+6}_{-4}	16^{+8}_{-6}	18^{+7}_{-6}	10^{+10}_{-6}	Chandra	9
	2,458,792.5	11^{+5}_{-4}	12^{+7}_{-5}	26^{+10}_{-8}	22^{+14}_{-5}	Chandra	9
	2,459,151.0	7^{+4}_{-3}	9^{+7}_{-5}	8^{+4}_{-3}	10^{+10}_{-5}	Chandra	9
	Mean Flux	10 ± 1	11 ± 2	16 ± 4	12 ± 2	⋯	
PSS 0926+3055	2,452,344.5	33^{+8}_{-6}	33^{+9}_{-7}	52^{+12}_{-10}	53^{+27}_{-7}	Chandra	5, 11
	2,453,322.5	39 ± 3	⋯	⋯	⋯	XMM-Newton	5
	2,455,623.5	31^{+8}_{-7}	32^{+10}_{-8}	46^{+12}_{-10}	42^{+25}_{-8}	Chandra	7
	2,455,939.5	24^{+8}_{-6}	23^{+9}_{-7}	23^{+8}_{-6}	31^{+22}_{-7}	Chandra	7
	2,456,424.5	39^{+9}_{-8}	47^{+13}_{-11}	73^{+18}_{-15}	60^{+29}_{-11}	Chandra	8
	2,456,675.5	39^{+10}_{-9}	41^{+12}_{-10}	49^{+13}_{-11}	40^{+25}_{-10}	Chandra	8
	2,458,186.5	14^{+6}_{-5}	17^{+11}_{-7}	50^{+21}_{-16}	40^{+25}_{-7}	Chandra	9
	2,458,491.5	51^{+15}_{-12}	52^{+18}_{-15}	47^{+14}_{-12}	49^{+28}_{-15}	Chandra	9
	2,458,873.5	30^{+10}_{-8}	36^{+17}_{-13}	87^{+28}_{-23}	62^{+31}_{-13}	Chandra	9
	Mean Flux	33 ± 4	35 ± 4	53 ± 7	47 ± 4	⋯	
PSS 1326+0743	2,452,284.5	28^{+7}_{-6}	28^{+8}_{-6}	42^{+10}_{-8}	48^{+24}_{-6}	Chandra	5, 11
	2,453,001.5	28^{+2}_{-3}	⋯	⋯	⋯	XMM-Newton	5
	2,455,627.5	29^{+8}_{-7}	32^{+10}_{-8}	50^{+14}_{-11}	38^{+24}_{-8}	Chandra	7
	2,456,047.5	33^{+9}_{-7}	35^{+11}_{-9}	48^{+13}_{-11}	47^{+26}_{-9}	Chandra	7
	2,456,632.5	31^{+10}_{-8}	32^{+11}_{-9}	18^{+6}_{-5}	16^{+18}_{-9}	Chandra	8
	2,456,729.0	49^{+12}_{-10}	45^{+13}_{-11}	42^{+10}_{-9}	56^{+29}_{-11}	Chandra	8
	2,458,239.0	26^{+9}_{-7}	33^{+14}_{-11}	47^{+16}_{-13}	41^{+25}_{-11}	Chandra	9
	2,458,603.5	42^{+12}_{-10}	44^{+17}_{-14}	75^{+21}_{-17}	86^{+35}_{-14}	Chandra	9
	2,458,934.5	35^{+13}_{-10}	34^{+16}_{-12}	46^{+17}_{-13}	40^{+26}_{-12}	Chandra	9
	Mean Flux	33 ± 3	35 ± 2	46 ± 5	46 ± 7	⋯	

Note. Mean fluxes are calculated over all epochs and observatories with uncertainties $\sigma/\sqrt{N_{\mathrm{obs}}}$, where σ is the standard deviation of the light curve. See Section 3.4 for mean fluxes over only Chandra epochs.
References. (1) Bechtold et al. (1994); (2) Kaspi et al. (2000); (3) Vignali et al. (2001); (4) Ferrero & Brinkmann (2003); (5) Shemmer et al. (2005); (6) Grupe et al. (2006); (7) Paper I; (8) Paper II; (9) this work; (10) Grupe et al. (2004); (11) Vignali et al. (2003).
[a] Galactic-absorption-corrected flux estimated by manual modeling in `Sherpa` (left) and using CIAO's automated *srcflux* script (right).

Using these simulations, we obtained three sets of 1000 χ^2 values for artificial *nonvariable* light curves of each of our four sources: (1) for all epochs in the soft band, (2) Chandra epochs in the soft band, and (3) Chandra epochs in the hard band. The distribution densities of the simulated χ^2 values are presented in Figure 2, along with the normal distribution expected from the values, and the statistical properties of each distribution are reported in Table 4. In all cases, the median of the normal distribution is higher than that of the actual distribution, showing the potential bias of higher χ^2 values for our light curves in the Gaussian limit.

To address this discrepancy, our variability classification is based on the distribution of simulated values rather than the normal distribution that the standard χ^2 *p*-value (the probability
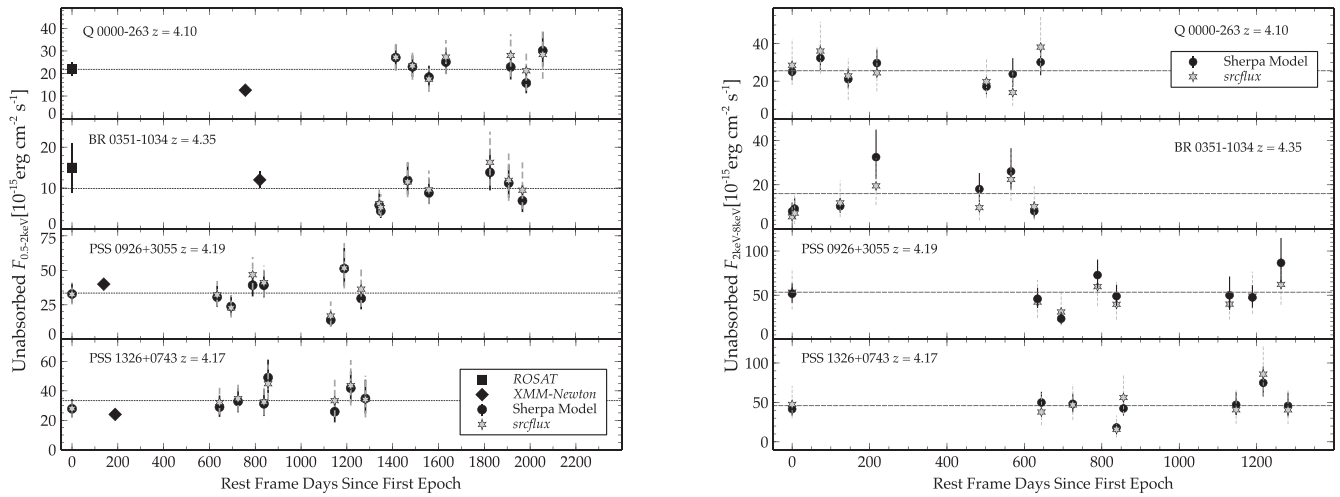
Figure 1. Galactic-absorption-corrected flux in the 0.5–2 keV (left) and 2–8 keV (right) observed-frame bands plotted as a function of days in the rest frame. Squares, diamonds, circles, and gray stars represent ROSAT, XMM-Newton, Chandra (obtained with Sherpa), and Chandra (obtained with srcflux) observations, respectively. Dotted lines represent the average flux over the light curve (using the Sherpa Chandra fluxes). Both methods of obtaining flux are consistent, within the uncertainties (90%), in all cases, however, the uncertainties in the srcflux fluxes are ∼33% (∼80%) larger than the Sherpa fluxes in the soft (hard) band. Note that only the Chandra observations are shown in the hard band, and therefore the zero-day points differ between the soft- and hard-band light curves for Q0000−263 and BR 0351−1034.

by which the null hypothesis of nonvariability can be rejected) represents. Our p-value based on the simulations, p_s, represents the fraction of χ^2 in the respective source's simulated distribution that is smaller than the observed χ^2 score. Therefore, an observed χ^2 score greater than 90% of the simulated scores (i.e., $p_s \geqslant 0.90$) allows us to reject the null hypothesis of nonvariability at 90% confidence.

Table 5 reports the results of the χ^2 tests, their respective degrees of freedom (dof; where dof $= N_{obs} - 1$), and p_s, for the soft band and hard band, respectively. When compared to the distribution of nonvariable χ^2 scores in the simulations, the only source for which we can reject the nonvariable hypothesis over all epochs is PSS 0926+3055, with a score greater than 99% of the simulated values. When considering only Chandra epochs, both Q0000−263 and PSS 0926+3055 are variable with $p_s = 0.99$ and $p_s = 0.90$, respectively, in the soft band. In the hard band, with the exception of Q0000−263, all sources are variable, and quite notably, both PSS 0926+3055 and PSS 1326+0734's observed χ^2 scores were larger than 100% of the simulated values. We consider all four sources variable in at least one band and PSS 0926+3055 in both.

We also performed similar Monte Carlo simulations and χ^2 analysis on the Γ_{eff} values reported in Table 2 (see also Table B1 for recomputed Γ_{eff} values from Papers I and II). None of the sources show significant spectral variability in Γ_{eff} ($\langle p_s \rangle = 0.08$), where $\langle p_s \rangle$ is the mean p_s for all four Chandra sources.

It should be stressed that a change in X-ray variability classification of these sources is not necessarily an assignment of a physical secular characteristic to the source. Rather, it is a trend that has emerged as the light-curve resolution increases, and it is limited to the scope of our monitoring program. To say that these sources were not previously X-ray variable yet are behaving so now would be an incorrect assumption. In fact, it has been shown that changes in variability classification should be expected as the number of net counts per source increases (see, e.g., Gibson & Brandt 2012, P17).

3.1.2. Variability Amplitude

To quantify the variability amplitude, Papers I and II measured the excess variance, σ_{rms}^2, of each source's light curve. This quantity provides a measurement of the fraction of variable flux in each epoch, after subtracting statistical uncertainty. Both the excess variance and its uncertainty are reported in Table 5, for the soft and hard bands. Following Turner et al. (1999), σ_{rms}^2 is defined as

$$\sigma_{rms}^2 = \frac{1}{N_{obs}\langle f \rangle^2}\sum_{i=1}^{N_{obs}}[(f_i - \langle f \rangle)^2 - \sigma_i^2], \quad (2)$$

where the result can be negative if the measurement errors are larger than the fraction of variable flux. The formal error[19] on this value is $s_D / \langle f \rangle^2 \sqrt{N_{obs}}$, where

$$s_D^2 = \frac{1}{N_{obs} - 1}\sum_{i=1}^{N_{obs}}\{[(f_i - \langle f \rangle)^2 - \sigma_i^2] - \sigma_{rms}^2 \langle f \rangle^2\}^2. \quad (3)$$

The excess variance is consistent with zero, within its uncertainties, in all cases, with the exception of BR 0351−1034 in the hard band, where the variable flux is ∼40% of the total flux. BR 0351−1034 is our faintest and highest-redshift source. Consequently, observations of the object suffer from the lowest signal-to-noise ratio (S/N) of our sources, with the $\langle S/N \rangle$ being ∼2/3 of that of the full sample. Indeed, this source's hard-band χ^2 score is higher than 92% of simulations, and a nonzero result is expected; however, it should be noted that this source is subject to the highest degree of noise and statistical uncertainty among all four sources in both the soft and hard bands.

Another class of results is of interest: those cases where a source is considered variable based on p_s, although the excess variance is consistent with zero. This is the result in five of the six cases where $p_s \geqslant 0.90$, with the sixth being that of BR 0351−1034 discussed above. The stochastic nature of

---

[19] This expression for the error does not account for any scatter intrinsic to the red noise inherent in a typical AGN power spectral density (PSD) function (see, e.g., Vaughan et al. 2003; Allevato et al. 2013).
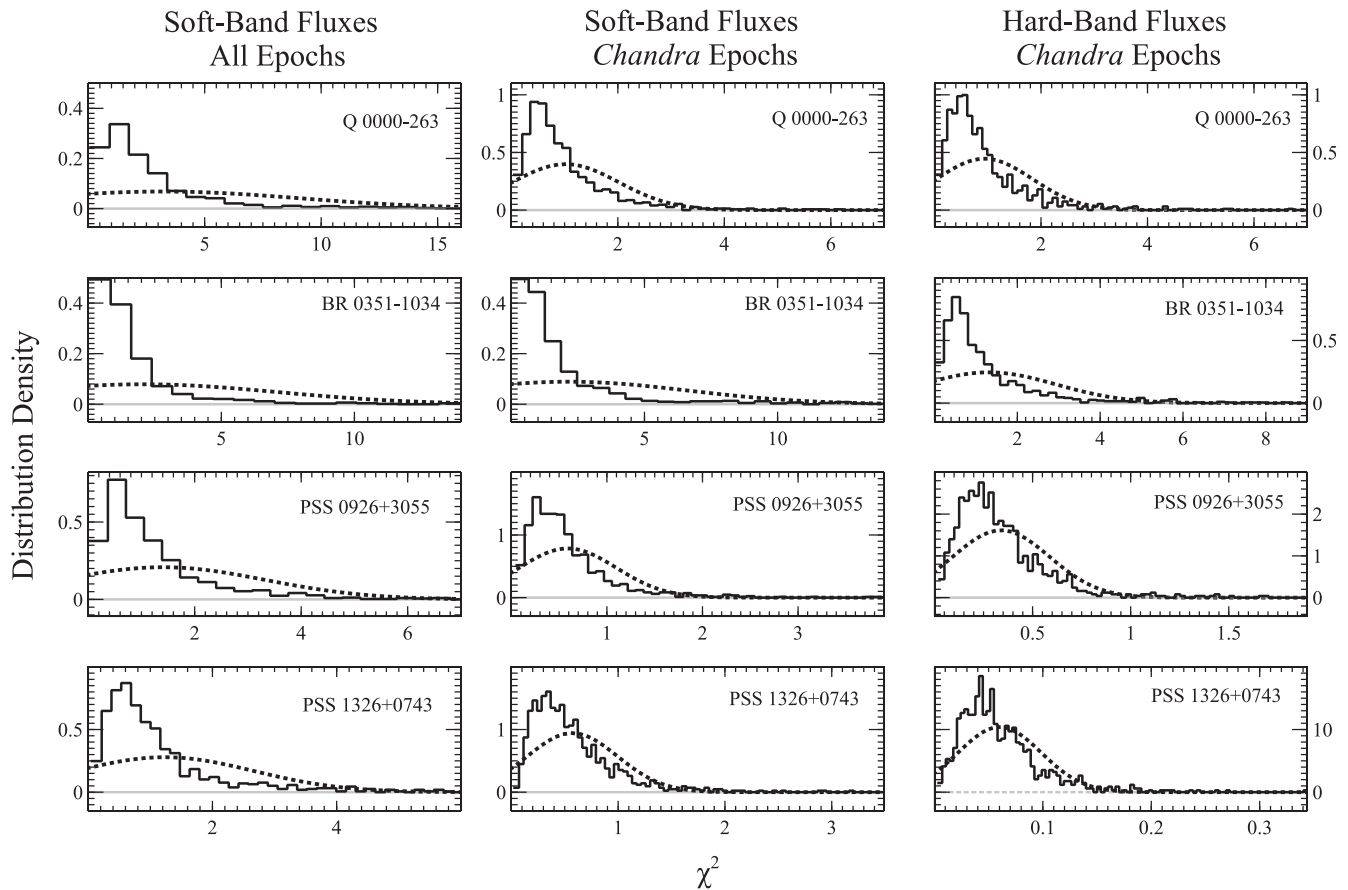
Figure 2. The results of the χ^2 simulations. The solid black line in each panel plots the distribution density of χ^2 statistic values from 1000 simulations of each object's light curve in the soft or hard band. The dotted line in each panel represents the distribution of χ^2 for each set of simulations expected from a normal distribution. In every case, the median of the normal distribution is higher than that of the actual distribution of the simulations, suggesting a bias toward larger χ^2 values in the Gaussian limit. Note that each plot is truncated to show at least 90% of the actual distribution.

AGN X-ray emission results in aperiodic red noise dependent on the shape of the PSD function. As a result, significant bias toward large scatter of $\sigma^2_{\rm rms}$ that diminishes as S/N increases has been shown in larger samples (see, e.g., CDF-S in Figure 4 of P17). This bias is quantifiable if a high-quality PSD is known for the source, which is not the case for our Chandra sources. While the S/N ratio is generally high enough for a reliable excess variance measurement, the assumed Gaussian errors and low net counts per source raise the magnitude of statistical uncertainty to that of the measured $\sigma^2_{\rm rms}$. Calculating the excess variance and its uncertainty in the simulated light curves shows that our low-count and sparsely sampled sources are subject to a bias toward negative values, with over 98% of simulated $\sigma^2_{\rm rms} < 0$ and ~25%–50% of the upper limits yet still negative in the Chandra epochs.

Extreme care must be taken when using $\sigma^2_{\rm rms}$ on individual sources. In fact, estimates from individual light curves with low S/N ($\lesssim 3$) and those with sparsely sampled fluxes are highly unreliable. Further, those estimates made on light curves with the extreme sampling patterns, such as ours, are subject to even further uncertainty (see, e.g., Vaughan et al. 2003; Allevato et al. 2013). Our sample is not ideal for $\sigma^2_{\rm rms}$ statistics; however, we retain the results for comparison with our previously published results, based on fluxes obtained through Chandra PIMMS, as well as other similar samples.

3.2. Variability Timescales

Paper II presented the first qualitative assessment of variability timescales and patterns of RQQs at $z \simeq 4.2$ by means of a variability structure function (SF).[20] We expand on the ensemble SF presented in Paper II by adding three additional epochs, as well as present an individual SF for each of the four Chandra sources, in both the soft and hard bands. The ensemble SF was computed by averaging the SF values (i.e., Δm) of all four sources in each rest-frame time bin, according to the SF definition in Fiore et al. (1998),

$$\Delta m_{ji} = |2.5 \log[f(t_j)/f(t_i)]|, \qquad (4)$$

where $f(t_j)$ is the flux at epoch t_j and $f(t_i)$ is the flux at epoch t_i, where $t_j > t_i$, and every t_j is measured in rest-frame days since the first epoch, such that $t_i = 0$. The uncertainty on $\langle \Delta m \rangle$ is expressed as $\sigma/\sqrt{N_b}$, where σ is the standard deviation of Δm and N_b is the number of data points in the respective bin. For the Chandra sources, we also add an additional 30% uncertainty to $\langle \Delta m \rangle$ in quadrature to account for the X-ray photometric errors (see Section 3).

Time bins (T_B) were determined using the machine-learning-based `optbinning` Python package (Navas-Palencia 2020) and differ for each band and sample. It should be noted that the

---
[20] See Section 3.3 in Paper II on the use of SFs in the absence of a high-quality PSD function.

Table 4
Simulated χ^2 Statistics

| Quasar | Soft Band (0.5–2.0 keV) | | | | | | Hard Band (2.0–8.0 keV) | | |
| | All Epochs | | | Chandra Epochs | | | | | |
	$\langle\chi^2\rangle$	Min/Max	σ	$\langle\chi^2\rangle$	Min/Max	σ	$\langle\chi^2\rangle$	Min/Max	σ
Q0000−263	3.21	0.10/82.3	5.86	1.02	0.05/15.1	1.00	0.94	0.05/9.47	0.90
BR 0351−1034	2.07	0.07/77.1	5.06	2.15	0.04/60.6	4.48	1.31	0.03/19.4	1.62
PSS 0926+3055	1.40	0.03/33.9	1.92	0.59	0.06/8.35	0.51	0.34	0.03/2.53	0.25
PSS 1326+0743	1.23	0.06/15.8	1.43	0.57	0.03/4.26	0.42	0.06	<0.01/0.34	0.04

Note. σ is the standard deviation of the set of simulated χ^2 values.

time bins have changed from those used in Papers I and II. We find that these new time bins allow each region in the time domain to carry relatively consistent statistical weight, whereas the previously used bins were weighted in favor of longer timescales. Each time bin now contains 7–38 data points for the Chandra sources.

Figure 3 presents the ensemble SF of our Chandra sources against the ensemble SF of the luminous Swift sources at intermediate redshifts ($1.33 < z < 2.74$) from Paper I. Statistics for the time bins for the Chandra and Swift SFs are reported in Table 6. Given that the uncertainties on the Swift X-ray photometry are considerably smaller than those of Chandra (see Paper I), the uncertainties on the Swift SF do not contain a photometric component similar to that included in the Chandra SFs (i.e., the addition of such a component produced a negligible effect). In the soft and hard bands, we find that the Chandra SFs are consistent with or lower than that of the Swift SF, within the uncertainties, which is consistent with the results of Paper II. At all available timescales, the Chandra soft- and hard-band SFs are consistent within the uncertainties. Considering the behavior of soft- and hard-band flux from both the lower- and higher-redshift sources, X-ray variability evolution with redshift is not observed.

Figure 4 presents the SF for each Chandra source, in the same manner as the ensemble SF, for the soft (top) and hard (bottom) bands. The time bins and SF values are reported in Table 7. Nearly all SF values in each panel are consistent within the uncertainties, per object, at each timescale, and no clear trends of changing SF as a function of timescale are observed. Additional and more frequent observations of the sources are needed to constrain their behavior, particularly at the shorter timescales.

3.3. Stacked Images

The stacked Chandra images presented in Figure 5 (top) were created by first applying positional shifts to each observation. While Chandra's pointing accuracy is precise to $\sim 0\farcs4$, there are small deviations in the sources' recorded positions between observations. For each observation, the absolute astrometry was locked to each source's position in its first observation using the CIAO threads *wcs_match* and *wcs_update*. We then used the *reproject_obs* CIAO thread centered around each object's X-ray coordinates to combine the observations. The resulting stacked images of PSS 0926+3055 and PSS 1326+0743 contain observations from Chandra Cycles 3, 12–15, and 19–21, amounting to ~ 40 ks each (spanning ~ 1300 days in the rest frame), and Q0000−263 and BR 0351−1034 are composed of observations from Cycles

12–15 and 19–21, amounting to ~ 70 ks each (spanning ~ 700 days in the rest frame).

We utilize these images to search for extended X-ray emission or companion X-ray sources in proximity to our objects. To aid with visual inspection of non-point-like emission and companion sources, each stacked image was smoothed using the CIAO thread *csmooth*. The images, also presented in Figure 5 (bottom), were processed using a Gaussian kernel with a minimal (maximal) S/N of 2 (50), following Nanni et al. (2018) for low-count observations. As seen in Figure 5, BR 0351−1034 appears to exhibit extended emission in the southwest direction. However, the counts in this feature occupy $\sim 16\%$ of the annulus around the centroid and represent $\sim 13\%$ of the counts present in the total annulus, and, therefore we consider this feature negligible. Furthermore, there is no visible evidence for this feature in the smoothed images. All four sources exhibit point-like structures with no evidence of significant extended X-ray emission.

With the exception of PSS 0926+3055, none of the images revealed the presence of potential companion X-ray sources within $25''$ following a *wavdetect* search as described in Section 2 on the unsmoothed images. The search revealed an X-ray source (with $26.6^{+6.2}_{-5.1}$ and $12.6^{+4.7}_{-3.5}$ soft- and hard-band counts, respectively) $\sim 15''$ southeast of PSS 0926+3055 as can be seen in Figure 5. This source is listed in the NASA/IPAC Extragalactic Database (NED) as CXOGSG J092637.2 +305454 and is referenced in Wang et al. (2016) as an X-ray source, but the number of counts is insufficient for a classification or redshift measurement for this object. The source is not detected in any Sloan Digital Sky Survey (SDSS; Blanton et al. 2017) band, with upper limits of 23.13, 22.70, and 22.20 mag in the g', r', and, i' bands, respectively (5σ). The source is also not detected in observations conducted by the Optical Monitor instrument on board XMM-Newton (B-band lower detection limit of 20.7 mag, 5σ) while observing PSS 0926+3055 (Shemmer et al. 2005), suggesting a red, high-redshift, or highly obscured object.

Utilizing the Faint Images of the Radio Sky at Twenty cm (FIRST; Helfand et al. 2015) survey, the upper limits on the radio flux densities of the $2''$ regions around PSS 0926+3055 and its potential companion source are ~ 0.2 and ~ 0.3 mJy (1σ), respectively, at an observed-frame band of 1.4 GHz, where the typically adopted threshold for detection is ~ 1.0 mJy (5σ).

In order to assess the likelihood that the potential companion source is physically associated with our target quasar, we started by computing its mean flux. This was performed by using seven of the nine exposures in which the source was significantly detected (it is undetected in the Cycle 19 and 20

Table 5
X-Ray Variability Indicators

| | Soft Band (0.5–2.0 keV) | | | | | | Hard Band (2.0–8.0 keV) | | |
| | All Epochs | | | Chandra Epochs | | | | | |
Quasar	χ^2(dof)	$p_{\rm sim}$ [a]	$\sigma^2_{\rm rms}$	χ^2(dof)	$p_{\rm sim}$ [a]	$\sigma^2_{\rm rms}$	χ^2(dof)	$p_{\rm sim}$ [a]	$\sigma^2_{\rm rms}$
Q0000−263	20.7(8)	0.51	0.00 ± 0.02	0.77(6)	0.99	-0.02 ± 0.02	0.99(6)	0.69	-0.02 ± 0.02
BR 0351−1034	1.67(8)	0.64	-0.03 ± 0.05	1.50(6)	0.70	-0.03 ± 0.05	3.05(6)	0.92	0.15 ± 0.08
PSS 0926+3055	2.86(8)	0.99	0.03 ± 0.04	2.40(7)	0.90	0.03 ± 0.05	3.14(7)	1.00	0.03 ± 0.05
PSS 1326+0743	1.35(8)	0.74	0.00 ± 0.02	0.71(7)	0.74	-0.02 ± 0.02	0.82(7)	1.00	0.02 ± 0.06

Note.
[a] The fraction of simulated χ^2 values smaller than the observed statistic.
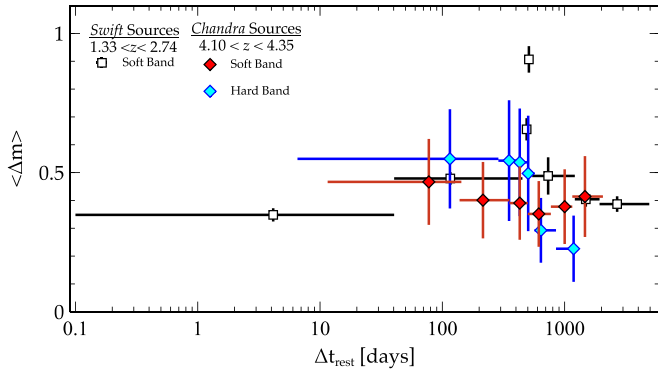
Figure 3. Ensemble SFs of our Chandra sources, for both the hard (blue diamonds) and soft (red diamonds) bands, compared to the ensemble SF of the Swift sources (soft band, squares) from Paper I. Averages of magnitude differences between all objects are plotted against time bins of rest-frame days between epochs. In every time bin where Swift and Chandra data are available, the soft- and hard-band Chandra SF is either lower than or consistent with the Swift SF, within the uncertainties. Time bins are weighted to have similar statistical weights.

Table 6
Ensemble Structure Function Time Bin Statistics

$T_{B,\rm min}$	$T_{B,\rm median}$	$T_{B,\rm max}$	N_b [a]	$\langle \Delta m \rangle$
	Swift Sources–Soft Band			
0.0	4.1	40.3	161	0.35 ± 0.02
40.4	116.2	451.7	234	0.48 ± 0.02
451.6	489.1	502.1	92	0.66 ± 0.04
502.1	510.3	543.2	77	0.91 ± 0.05
543.2	733.2	1211.6	166	0.49 ± 0.03
1211.6	1489.7	1929.9	154	0.40 ± 0.03
1929.9	2687.3	4922.2	80	0.37 ± 0.03
	Chandra Sources–Soft Band			
6.6	72.6	138.1	25	0.47 ± 0.15
138.0	214.9	354.3	22	0.40 ± 0.14
354.3	429.5	499.6	25	0.39 ± 0.13
499.6	614.7	771.7	33	0.35 ± 0.12
771.7	1000.8	1155.5	18	0.38 ± 0.13
1155.5	1466.2	2056.5	21	0.41 ± 0.15
	Chandra Sources–Hard Band			
6.6	115.4	287.4	38	0.55 ± 0.18
287.4	351.4	414.0	13	0.54 ± 0.22
413.9	429.5	492.7	13	0.54 ± 0.19
492.8	503.5	567.4	12	0.50 ± 0.21
567.4	639.7	850.4	15	0.29 ± 0.12
850.3	1184.4	1286.3	7	0.29 ± 0.12

Note. T_B in units of rest-frame days.
[a] Number of data points in the time bin.

exposures). Following the procedures of Section 2, we derived a mean flux for the source in the soft, hard, and full bands, by means of spectral fitting. We note, however, that since each of the seven exposures did not contain sufficient counts to fit a spectral model, the data from all seven exposures were combined and jointly fit with a single power-law model and a varying intrinsic absorption model (see Section 3.4). Using the mean fluxes, we computed the likelihood that one of our four sources would have a companion with at least the mean flux of the potential companion, in the soft, hard, and full bands, within a 15″ distance. The mean source flux in each band and the respective likelihoods, p_c, to 90% confidence are reported in Table 8, where p_c is computed using the flux-to-sky-density relation from Chen et al. (2018, see their Figure 13). The probability of finding a similar or brighter source within 15″ of one of our sources is small, although nonnegligible, with a mean p_c of 3.1% across all three bands.

The source's fluxes for each epoch were estimated using *srcflux* with the mean photon index and $N_{\rm H}$ from the combined spectral fit: $\Gamma_{0.5-10.0\,\rm keV} \sim 1.6$ and $N_{\rm H} \sim 2.7 \times 10^{20}\,\rm cm^{-2}$. The source's light curve was then simulated 1000 times (see Section 3.1.1), and following the χ^2 variability test, the source is not variable in the soft or hard band ($p_s = 0.50$ and $p_s = 0.57$, respectively). Follow-up multiwavelength observations of this source are required for its reliable classification.

3.4. Mean Spectra

Our X-ray observations were designed to provide only the minimum number of counts required for basic time-series analyses, and thus, alone, each observation does not provide a meaningful X-ray spectrum. However, a combination of all of the Chandra observations can give further insight as to the basic X-ray spectral properties of each source, as well as the accuracy of the individual fits used to calculate flux.

Our mean spectra were obtained using the CIAO thread *combine_spectra* to merge the spectrum from each level-2 event file into a mean spectrum for each object, and they are presented in Figure 6. X-ray spectral fitting was performed using Sherpa to fit a single power-law model with a Galactic absorption component (xsphabs×xspowerlaw). The photon indices were determined by minimization of the *cstat* statistic with the spectra grouped to a minimum of one count per energy bin. Ratios are presented as data/model.
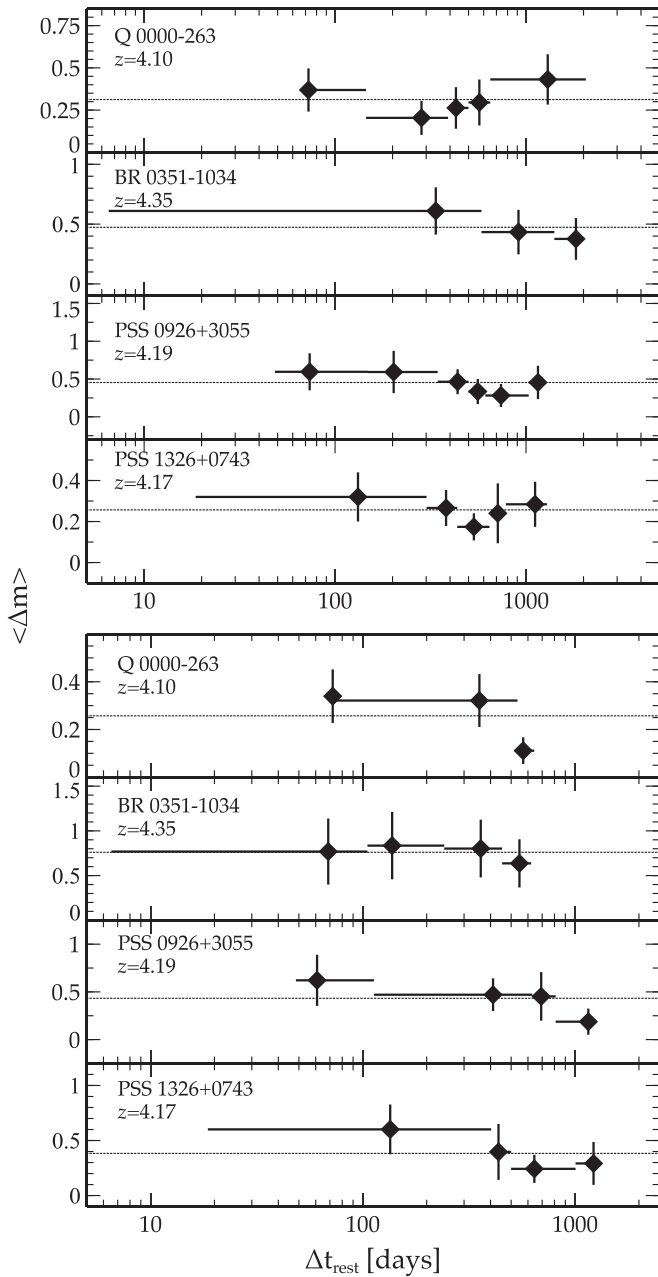
Figure 4. SF of each Chandra object in the 0.5–2 keV band (top) and 2–8 keV band (bottom) plotted as average magnitude differences against time bins as prescribed in Fiore et al. (1998). Soft-band SFs contain data from Chandra, XMM-Newton, and ROSAT. Hard-band SFs contain only Chandra data. The dotted line in each panel represents the mean SF. Time bins were constructed to hold similar statistical weights. Within the uncertainties, nearly all points of the SFs are consistent with their respective mean in both the soft and hard bands.

Due to the cycle-to-cycle decay in the X-ray ultrasoft band (see Appendix A), our spectra were only fit across the observed-frame energy range 0.5–8 keV. The photon indices we obtain from the stacked Chandra data are consistent, within the 90% uncertainties, with the values obtained from XMM-Newton imaging spectroscopy of the sources using a similar model (fit over 0.2–10 keV; Shemmer et al. 2005) roughly three rest-frame years earlier, and they are reported in Table 9. Also reported in Table 9 is a model-based estimate of the mean soft- and hard-band flux for each object, calculated with the model component xscflux, and the net counts ($N_{0.5-2.0\ keV} + N_{2-8\ keV}$) for each source. All mean fluxes from

the stacked spectra are consistent, within the uncertainties, with the mean fluxes computed from the individual observations in Table 3.

Our sources' photon indices are consistent with those of typical type 1 AGNs ($\Gamma \sim 1.9$ up to $z \sim 7$). Luminous quasar spectra have been individually and jointly fit up to $z \sim 7$ and show relatively consistent behavior (see, e.g., Piconcelli et al. 2005; Vignali et al. 2005; Shemmer et al. 2006b; Just et al. 2007; Nanni et al. 2017; Vito et al. 2019; Wang et al. 2021).

3.5. Ground-based Photometry

With the exception of the Cycle 19 observations of Q0000 −263 and BR 0351−1034, all the Chandra observations were complemented by near-simultaneous optical–UV observations to search for similar behaviors in X-ray and rest-frame UV variability. The ground-based observations were performed at the Tel Aviv University Wise Observatory (WO), utilizing the 1 m (WO 1m), C18 18-inch (WOC18), and C28 28-inch (WOC28) telescopes, the Las Campanas Observatory, using the du Pont 2.5 m telescope (LCO-dP), and the Las Cumbres Observatory using the 1 m telescope (LCO-1m). The properties of each detector used are reported in Table 10. Depending on availability per night, each observatory used the SDSS u', g', r', i', and z' filters (Fukugita et al. 1996) and the Bessel B, V, R and I filters (Bessell et al. 1998).

The same analysis procedures used in Papers I and II were followed to obtain the calibrated magnitudes and rest-frame UV flux densities, which are reported in Tables 11 and 12, respectively. The light-curve calibration is done on the entire set of observations, rather than each individual image. Therefore, each new observation has the potential of showing a systematic change in magnitudes for all previous observations. Between Papers I and II, only two nonnegligible, but small (i.e., consistent with the original values at the $\sim 2\sigma$ level), changes were reported. All values reported in Paper II are consistent with those calculated after recalibration in this work, and they are left unchanged in Table 11.

3.5.1. Optical–UV Variability

To test for variability in the optical–UV bands, the χ^2 variability test was applied to the light curve of each band with over three observations, per object, as well as measurement of the respective variability amplitude. The 90% confidence level in the X-ray analysis was selected owing to the large uncertainty in the flux estimates ($\sim 30\%$) driven by the low-count photon statistics. The optical/UV flux measurements are comparatively more accurate (generally $\lesssim 0.1\%$ uncertainty), and we therefore adopt a variability criterion of $p \geqslant 99\%$.

Variability is considered a property of a source's entire light curve, rather than a property of individual events at specific points in the light curve. In order to maintain the qualitative nature of a band being variable, the χ^2 and σ^2_{rms} results need to be considered independently, as well as together. In some cases, σ^2_{rms} and its uncertainty are inconsistent with zero, suggesting variability, but the χ^2 result does not allow us to reject the null hypothesis confidently. Similarly, in some other cases, the χ^2 result allows us to reject the nonvariable null hypothesis, though the variability amplitude is consistent with zero within its uncertainty. Each of these cases was inspected epoch by epoch to see whether variability was a general trend in the light curve, or whether a single event (i.e., a one-time

Table 7
Individual Structure Function Time Bin Statistics

Quasar	Soft Band (0.5–2.0 keV)					Hard Band (2.0–8.0 keV)				
	$T_{B,\min}$	$T_{B,\mathrm{median}}$	$T_{B,\max}$	N_b[a]	Δm	$T_{B,\min}$	$T_{B,\mathrm{median}}$	$T_{B,\max}$	N_b[a]	Δm
Q0000−263	67.8	72.6	145.3	7	0.37 ± 0.13	67.8	72.2	73.1	4	0.34 ± 0.11
	145.3	283.5	390.4	5	0.20 ± 0.10	73.1	354.3	535.7	14	0.32 ± 0.11
	390.4	429.4	499.6	5	0.26 ± 0.12	535.7	569.8	642.0	3	0.11 ± 0.06
	499.6	569.6	649.6	4	0.30 ± 0.14	...	...	...	...	...
	649.6	1299.2	2056.5	15	0.43 ± 0.15	...	...	...	...	...
BR 0351−1034	6.5	336.8	584.2	21	0.61 ± 0.20	6.5	68.7	105.1	4	0.77 ± 0.37
	684.2	912.9	1407.4	10	0.43 ± 0.19	105.1	137.5	241.9	5	0.84 ± 0.38
	1407.4	1825.8	1963.3	5	0.38 ± 0.17	241.9	359.6	453.4	5	0.80 ± 0.32
	...	...	...	...	...	453.4	547.1	621.2	7	0.64 ± 0.27
PSS 0926+3055	48.4	73.6	148.1	7	0.60 ± 0.24	48.4	60.9	112.9	5	0.62 ± 0.27
	148.1	202.7	344.7	5	0.59 ± 0.28	112.9	410.9	629.0	16	0.47 ± 0.17
	344.7	438.2	499.0	8	0.46 ± 0.17	629.0	692.7	810.3	3	0.45 ± 0.25
	499.0	559.0	612.0	4	0.33 ± 0.17	810.3	1155.0	1258.0	4	0.19 ± 0.14
	612.0	739.4	1032.8	8	0.28 ± 0.15	...	...	...	...	...
	1032.8	1155.0	1258.0	4	0.46 ± 0.22	...	...	...	...	...
PSS 1326+0743	18.7	131.8	301.3	11	0.32 ± 0.12	18.7	134.6	402.5	13	0.60 ± 0.23
	301.3	381.2	435.9	5	0.27 ± 0.09	402.5	435.9	499.7	4	0.40 ± 0.25
	435.9	533.2	643.1	8	0.17 ± 0.07	499.7	643.1	1005.7	8	0.24 ± 0.13
	643.1	711.7	784.4	4	0.24 ± 0.15	1005.7	1222.2	1286.3	3	0.29 ± 0.19
	784.4	1115.6	1286.3	8	0.28 ± 0.11	...	...	...	...	...

Note. T_B in units of rest-frame days.
[a] Number of data points in the time bin.

decrease or increase in flux) caused the disagreement between the tests. If a single event was responsible and the remaining epochs produced consistent results in both tests, the band was *not* considered variable.

The following objects are considered variable, at $> 99\%$ confidence, in the following bands: Q0000−263 in g', r', V and R; PSS 0926+3055 in g', r', V, R, and I; and PSS 1326+0743 in g'. The first half of epochs in the single band in which BR 0351−1034 was determined variable (g') was subject to errors four times larger than the later epochs, which makes it difficult to determine the reliability of the test results: $p > 0.99$, $\sigma_{\mathrm{rms}}^2 = 0.05 \pm 0.03$. With the exception of BR 0351−1034, the mean variability amplitude of the Chandra sources was < 0.01 in all tested bands. In general, the Chandra sources appear optically variable at a level of < 0.1 mag on rest-frame timescales of $\sim$2–3 months.

3.5.2. UV Flux Density and Optical-to-X-Ray Spectral Slope

Rest-frame UV flux densities at 1450 Å are reported in Table 12 for each ground-based epoch. The band used to calculate the flux density was chosen to minimize emission-line contamination at the rest-frame wavelength, while providing the smallest difference between the band wavelength and $1450(1 + z)$ Å, and maintaining the highest S/N. Once a band was selected, the flux density at a rest-frame wavelength of 1450 Å was extrapolated from the flux density at the effective wavelength of the respective band by assuming a quasar continuum of the form $f_\lambda \propto \lambda^{-1.5}$ (corresponding to $f_\nu \propto \nu^{-0.5}$; Vanden Berk et al. 2001). Magnitude zero-points used in the magnitude-to-flux conversions were obtained from Fukugita et al. (1996) and Bessell et al. (1998). With the exception of Q0000−263 ($p = 0.93$), all the sources are variable in $F_{1450\,Å}$ at $> 99\%$ confidence.

Extrapolating the rest-frame 2500 Å flux density, along with the rest-frame 2 keV flux density ($f_{2\,\mathrm{keV}}$, Table 2; also see Table B1) and its uncertainty (derived from the soft-band fluxes in Table 3), we compute the optical-to-X-ray spectral slope, α_{OX}, defined as $\log(f_{2\,\mathrm{keV}}/f_{2500\,Å})/\log(\nu_{2\,\mathrm{keV}}/\nu_{2500\,Å})$, and report the results in Table 12.

Also reported in Table 12 are the rest-frame time separations, Δt, between the X-ray and corresponding optical–UV observations. These time separations were kept as small as possible and are all on the order of ≈ 1 day in the rest frame. The α_{ox} measurements are also presented in Figure 7 as a function of rest-frame days since the first optical observation. Paper II reported a significant change in α_{OX} at a level of $\Delta\alpha_{\mathrm{OX}} = 0.08$ and $\Delta\alpha_{\mathrm{OX}} = 0.09$ between cycle pairs for Q0000−263 and PSS 0926+3055, respectively. After X-ray fluxes were estimated using Sherpa and three new epochs were added, the previous results have changed for all sources as explained below.

The measurement corresponding to the Cycle 20 Q0000−263 observation is inconsistent with every other measurement, with the exception of the Cycle 14 measurement. The Cycle 20 Chandra observation exhibited a decrease of $\sim$32% ($\sim$52% at the lower limit) from the mean flux of this source, while the optical observation, $\sim$5 rest-frame hours later, deviated $< 1\%$ from the mean flux. The maximum variation is between Cycles 12 and 20 with $\Delta\alpha_{\mathrm{OX}} = 0.17$. BR 0351−1034 shows significant variations up to $\Delta\alpha_{\mathrm{OX}} = 0.26$; however, the source's low S/N should be considered when interpreting this result.

PSS 0926+3055 showed significantly consistent measurements until Cycle 19, which was an extreme in its X-ray light curve with a flux 57% lower than the mean. The Cycle 20 X-ray flux was 57% *higher* than the mean. Between Cycle pairs 19–20 and 20–21, we find $\Delta\alpha_{\mathrm{OX}} = 0.27$ and $\Delta\alpha_{\mathrm{OX}} = 0.21$,
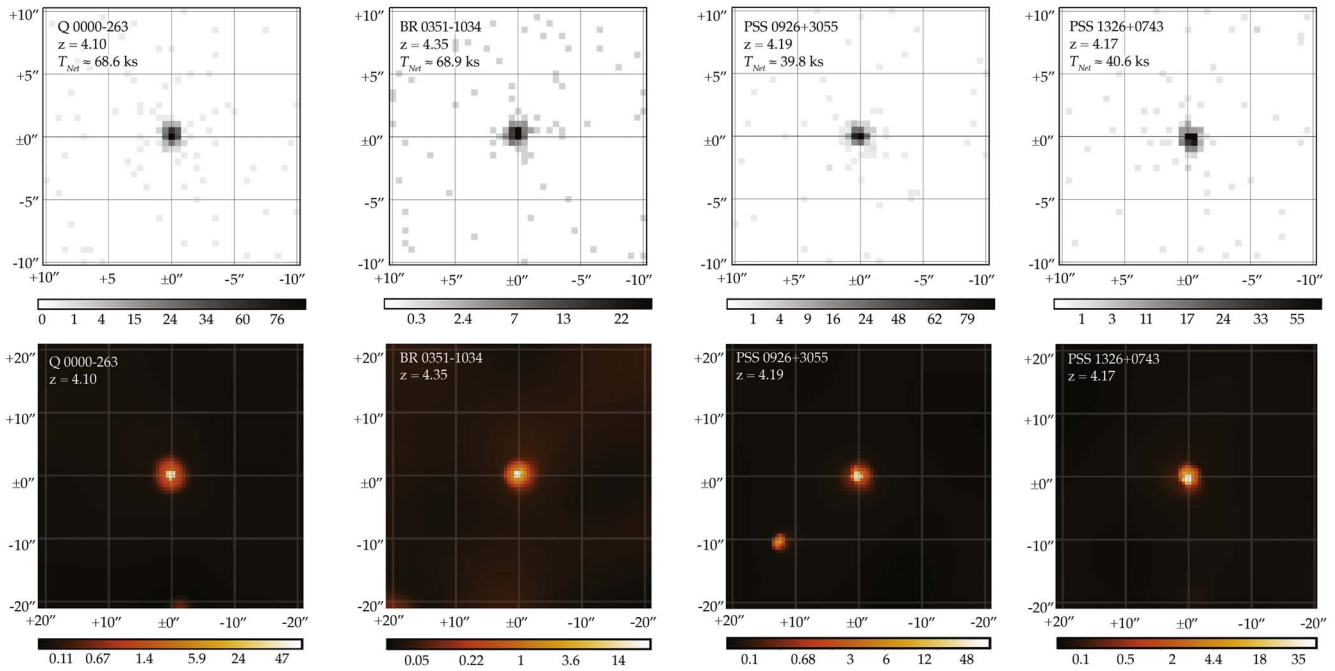
Figure 5. Top: stacked, $20'' \times 20''$ full-band images of our four objects spanning Cycles 12–15 and 19–21, providing an effective exposure time of $\sim$70 ks for Q0000 -263 and BR 0351$-$1034, and Cycles 3, 12–15, and 19–21, providing an effective exposure time of $\sim$40 ks for PSS 0926+3055 and PSS 1326+0743. Bottom: stacked, $40'' \times 40''$ full-band images of our four objects smoothed using the CIAO thread *csmooth* (see Section 3.3). In all panels, the grid is centered on the quasar's centroid, and the color bar represents the number of counts per pixel by brightness.

Table 8
Potential Companion Flux and Likelihood

Band[a]	Flux[b] (10^{-15} erg s^{-1} cm^{-2})	p_c[c]
Soft	$7.2^{+1.6}_{-1.4}$	$2.4^{+1.0}_{-0.5}$
Hard	$15.8^{+3.5}_{-3.1}$	$3.5^{+1.4}_{-1.1}$
Full	$23.0^{+5.1}_{-4.4}$	$3.1^{+1.1}_{-0.5}$

Notes.
[a] Hard- and full-band upper limits are 10 keV, rather than the 8 keV assumed in this work, for comparison with the results in Chen et al. (2018).
[b] Mean flux (90% confidence) measured with a single power-law fit on a combined spectrum using Sherpa.
[c] The probability of finding a source with at least the flux of PSS 0926+3055's potential companion within $15''$ of any of our sources in units of 10^{-2}.

respectively. In PSS 1326+0743, $\alpha_{\rm ox}$ shows no significant variability and the largest variation is $\Delta\alpha_{\rm ox} = 0.04$, which corresponds to the Cycle 14 flux density estimate rising 62% above the mean.

We find that variations in photon indices and X-ray flux produce most of the variation in $\alpha_{\rm ox}$, which supports findings that scatter in $\alpha_{\rm ox}$ is driven by X-ray variability (see, e.g., Paper I and references therein). However, the χ^2 test shows that $\alpha_{\rm ox}$ is not considered variable overall in each source (90% confidence), with the exception of PSS 0926+3055 ($p = 0.93$).

To further characterize the role of X-ray variability in the $\alpha_{\rm ox}$ scatter, we computed $\alpha_{\rm ox}$ with a constant photon index for each source across all epochs (i.e., with the *srcflux* fluxes). In this case, all four sources were formally nonvariable in $\alpha_{\rm ox}$ ($\langle p \rangle = 0.17$); however, we note that between the Cycle 13 and 14 observations of PSS 0926+3055, $\alpha_{\rm ox}$ showed a significant, yet small, variation at a level of $\Delta\alpha_{\rm ox} = 0.05$. These results suggest that if the photon index remains unchanged, changes in $\alpha_{\rm ox}$ are driven by X-ray flux variability.

The mild variations in $\alpha_{\rm ox}$ observed for our sources are consistent with observations of luminous, high-redshift quasars. For example, in an effort to tightly constrain $\alpha_{\rm ox}$ dispersion to use quasars as cosmological standard candles, Chiaraluce et al. (2018) showed that RQQs up to $z \sim 3.5$ show $\langle \Delta\alpha_{\rm ox} \rangle \sim 0.08$ on 10-to-100-day timescales (uncorrected for photometric uncertainty). Our sources behave consistently, on average, with their results with $\langle \Delta\alpha_{\rm ox} \rangle \sim 0.09 \pm 0.01$. While our results do not suggest increased $\alpha_{\rm ox}$ variability with redshift, the Chiaraluce et al. (2018) results, which are based on a much larger sample, leave a dispersion of $\Delta\alpha_{\rm ox} \sim 0.2$ unaccounted for by intrinsic source variability, and a redshift dependence is not ruled out (see also Lusso & Risaliti 2016).

4. Summary

We present three new X-ray epochs in a long-term time-series analysis of four luminous high-redshift ($z \approx 4.1 - 4.4$) RQQs, extending our temporal baseline to $\sim$1300 days in the rest frame for half of our sources and $\sim$2000 days in the rest frame for the other half. Our new X-ray observations were obtained with Chandra and are accompanied by near-simultaneous ground-based optical–UV observations. Our findings can be summarized as follows:

1. We find that two of our four sources, Q0000$-$263 and PSS 0926+3055, are X-ray variable in the soft band and three sources, BR 0351$-$1034, PSS 0926+3055, and PSS 1326+0743, are variable in the hard band.
2. There is no evidence for increased X-ray variability as redshift increases, bolstering our findings from Paper II. Hard-band X-ray variability is consistent with that of the soft band.
3. We do not observe significant changes in the SF of any of our Chandra sources across all timescales probed, and the ensemble SF of all four sources shows no indication for
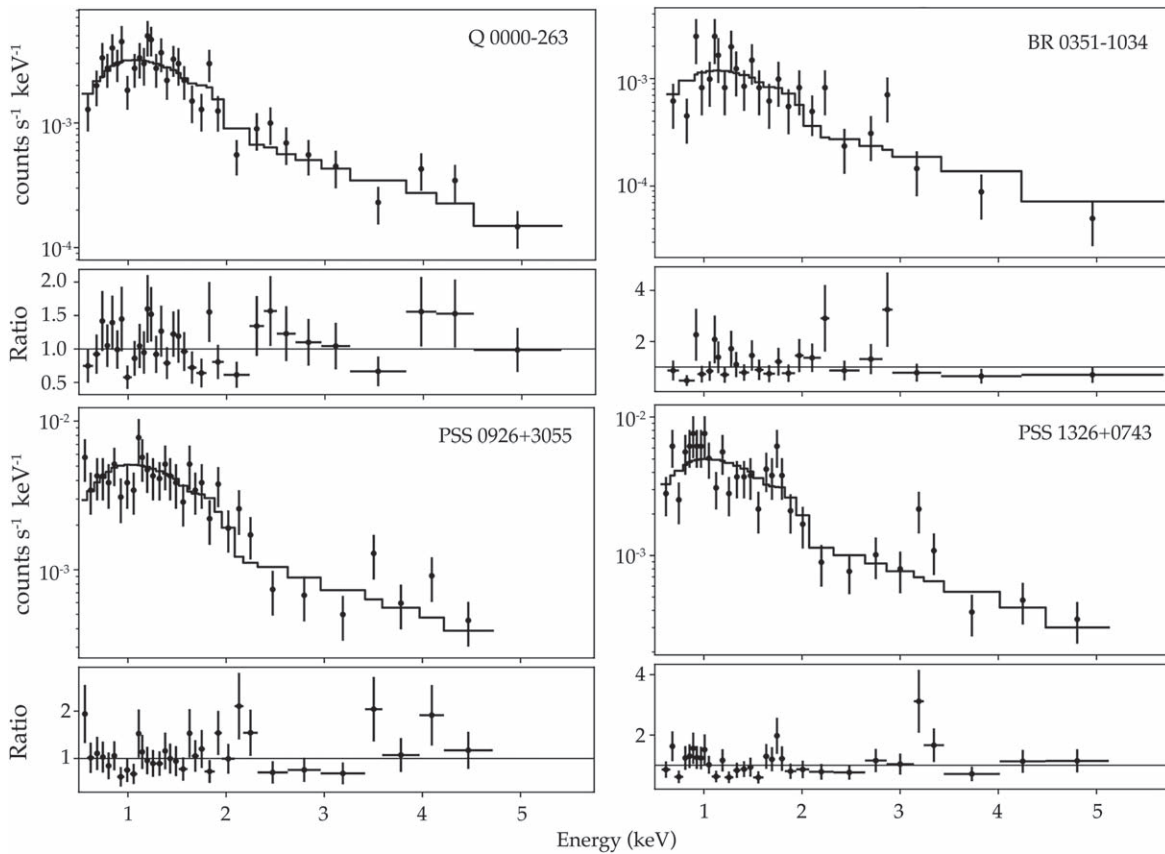
Figure 6. X-ray imaging spectroscopy from each Chandra observation combined to produce a mean spectrum for each source. Error bars are plotted at 90% confidence. Solid lines represent our best-fit models with Galactic-absorbed power-law models. Each spectral fit was modeled using the *cstat* statistic on data grouped into a minimum of one count per energy bin. Plotted below each spectrum is the ratio of the best-fit model (i.e., data/model). The spectra were binned for presentation purposes into groups of nine counts, except for our faintest source, BR 0351−1034, for which the data are binned into groups of five counts. For all four objects, the photon indices obtained with Chandra are consistent, within the errors, with the values obtained from the corresponding XMM-Newton observations (Shemmer et al. 2005), as well as the general type 1 AGN population up to $z \sim 7$, and are reported in Table 9.

<table>
<tr><td colspan="5" align="center">**Table 9**
Properties of Mean Spectra</td></tr>
</table>

	Flux[a] $(10^{-15}$erg s^{-1}cm$^{-2})$			
Quasar	$f_{0.5-2\ \mathrm{keV}}$	$f_{2-8\ \mathrm{keV}}$	Γ_{eff}[a]	C_ν[b](dof)/N_{net}[c]
Q0000−263	24 ± 2	24 ± 2	1.98 ± 0.16	1.13(154)/332
BR 0351−1034	9 ± 1	11^{+4}_{-3}	1.85 ± 0.26	0.73(96)/128
PSS 0926+3055	33 ± 4	45 ± 4	1.79 ± 0.17	0.96(164)/320
PSS 1326+0743	33 ± 3	43 ± 4	1.81 ± 0.16	0.82(165)/320

Notes.
[a] 90% confidence.
[b] The reduced *cstat* statistic (C/dof) as a goodness-of-fit measurement (Kaastra 2017).
[c] Net source counts (soft+hard) over all Chandra epochs.

<table>
<tr><td colspan="4" align="center">**Table 10**
Ground-based Telescope Properties</td></tr>
</table>

Telescope	Detector (CCD)	FOV	Spatial Scale (arcsec pixel^{-1})
WO 1m[a]	PI VA1300B	$13' \times 13'$	0.58
	SBIG STX16803	17.82×17.82	0.78
WOC18[a]	QSI 683	48.9×36.8	0.88
WOC28[a]	FLI PL16801	56.9×56.9	0.83
LCO-dP[b]	Wide Field	$25'$ Diameter	0.48
LCO-1m[c]	Sinistro	26.5×26.5	0.39

Notes.
[a] https://physics.tau.ac.il/astrophysics/wise_observatory_manuals
[b] http://www.lco.cl/?epkb_post_type_1=wide-field-reimaging-ccd-camera-wfccd
[c] https://lco.global/observatory/instruments/sinistro/

increased X-ray variability as redshift increases. At all timescales, the soft-band ensemble SF is consistent with or lower than that of the similarly luminous Swift sources. The hard-band ensemble SF is consistent with the Swift sources at longer timescales but is highly uncertain at shorter timescales.

4. The stacked Chandra image of PSS 0926+3055 reveals a nonvariable X-ray point source $\sim 15''$ southeast of the target quasar. While present in a Chandra point-source catalog, there is currently no record of this source in any other catalog. Additional multiwavelength observations, aimed particularly at measuring the redshift of this source, are required to determine whether it is a companion of PSS 0926+3055.

5. Mean photon indices of our sources, measured from their stacked Chandra spectra, are consistent, within the uncertainties, with those obtained ~ 3 rest-frame years prior with XMM-Newton, and with the mean photon index of AGNs observed to $z \sim 7$.

Table 11
Ground-based Photometry

Quasar	Obs.[a]	Obs. Date	g′ (mag)	r′ (mag)	i′ (mag)	z′ (mag)	B (mag)	V (mag)	R (mag)	I (mag)
Q0000−263	WO1m	2011 Sep 4	18.93 ± 0.02	17.45 ± 0.02	⋯	⋯	19.58 ± 0.04	18.23 ± 0.02	17.16 ± 0.02	⋯
	WO1m	2012 Sep 14	18.93 ± 0.03	17.48 ± 0.01	⋯	⋯	19.45 ± 0.09	18.28 ± 0.02	17.18 ± 0.03	⋯
	WO1m	2012 Sep 15	18.97 ± 0.02	17.48 ± 0.01	⋯	⋯	19.53 ± 0.04	18.26 ± 0.02	17.17 ± 0.01	⋯
	WOC18	2013 Sep 5	⋯	⋯	⋯	⋯	19.62 ± 0.10	18.37 ± 0.04	17.21 ± 0.02	⋯
	WOC18	2014 Sep 19	⋯	⋯	⋯	⋯	⋯	18.18 ± 0.04	17.07 ± 0.03	⋯
	WOC18	2014 Sep 20	⋯	⋯	⋯	⋯	19.40 ± 0.06	18.14 ± 0.04	17.09 ± 0.02	⋯
	LCO-dP	2014 Sep 26	⋯	⋯	⋯	⋯	⋯	17.97 ± 0.14	⋯	⋯
	WOC28	2019 Aug 13	18.71 ± 0.10	⋯	⋯	⋯	⋯	⋯	16.97 ± 0.04	⋯
	LCO-1m	2020 Aug 21	18.68 ± 0.05	17.23 ± 0.02	⋯	⋯	⋯	⋯	⋯	⋯
BR 0351−1034	WO1m	2011 Mar 3	⋯	19.39 ± 0.06	⋯	⋯	⋯	⋯	19.24 ± 0.05	⋯
	WO1m	2011 Mar 5	⋯	19.33 ± 0.04	⋯	⋯	⋯	⋯	⋯	⋯
	WO1m	2011 Sep 26	⋯	19.33 ± 0.03	⋯	⋯	⋯	20.59 ± 0.09	19.29 ± 0.04	⋯
	LCO-dP	2011 Oct 29	⋯	⋯	⋯	⋯	22.79 ± 0.11	20.55 ± 0.02	19.35 ± 0.03	⋯
	LCO-dP	2013 Aug 4	⋯	⋯	⋯	⋯	22.46 ± 0.06	20.36 ± 0.04	⋯	⋯
	WO1m	2013 Aug 18	⋯	⋯	⋯	⋯	⋯	20.39 ± 0.09	19.23 ± 0.08	⋯
	WO1m	2014 Nov 25	⋯	⋯	⋯	⋯	⋯	20.54 ± 0.11	19.14 ± 0.06	⋯
	LCO-dP	2014 Nov 26	⋯	⋯	⋯	⋯	⋯	20.41 ± 0.04	19.10 ± 0.04	⋯
	WO1m	2014 Nov 26	⋯	⋯	⋯	⋯	22.51 ± 0.08	⋯	⋯	⋯
	WOC18	2019 Nov 2	20.38 ± 0.31	18.98 ± 0.12	⋯	⋯	⋯	⋯	⋯	⋯
	WOC18	2019 Nov 3	20.34 ± 0.26	19.26 ± 0.11	⋯	⋯	⋯	⋯	⋯	⋯
	WOC28	2019 Nov 19	⋯	19.37 ± 0.08	⋯	⋯	⋯	⋯	⋯	⋯
	LCO-1m	2020 Nov 6	20.93 ± 0.07	19.18 ± 0.03	⋯	⋯	⋯	⋯	⋯	⋯
	LCO-1m	2020 Nov 9	21.16 ± 0.08	⋯	⋯	⋯	⋯	⋯	⋯	⋯
PSS 0926+3055	WO1m	2011 Mar 4	18.45 ± 0.01	17.13 ± 0.01	17.01 ± 0.01	17.22 ± 0.03	⋯	17.83 ± 0.02	16.90 ± 0.01	16.60 ± 0.02
	WO1m	2012 Feb 4	18.55 ± 0.05	17.23 ± 0.04	17.05 ± 0.05	⋯	⋯	17.94 ± 0.05	17.11 ± 0.08	16.66 ± 0.04
	WO1m	2013 May 15	⋯	⋯	⋯	⋯	19.20 ± 0.07	17.91 ± 0.01	16.92 ± 0.01	16.58 ± 0.01
	WO1m	2014 Jan 23	18.43 ± 0.03	17.13 ± 0.02	17.00 ± 0.02	⋯	⋯	17.91 ± 0.03	16.91 ± 0.02	16.41 ± 0.02
	WO1m	2018 Mar 9	⋯	17.36 ± 0.01	17.13 ± 0.01	17.14 ± 0.13	18.14 ± 0.01	18.14 ± 0.01	17.09 ± 0.06	16.76 ± 0.06
	WO1m[b]	2018 Mar 11	⋯	⋯	⋯	17.18 ± 0.13	19.43 ± 0.09	18.08 ± 0.08	17.07 ± 0.08	16.69 ± 0.06
	WOC28	2019 Jan 10	⋯	17.18 ± 0.05	17.02 ± 0.03	17.07 ± 0.06	⋯	⋯	⋯	⋯
	LCO-1m	2020 Feb 2	18.56 ± 0.01	17.15 ± 0.03	17.04 ± 0.01	17.06 ± 0.01	⋯	⋯	⋯	⋯
PSS 1326+0743	WO1m	2011 Mar 8	19.15 ± 0.10	⋯	⋯	⋯	⋯	18.47 ± 0.03	17.48 ± 0.02	16.88 ± 0.03
	WO1m	2011 Mar 14	19.28 ± 0.03	17.82 ± 0.10	17.51 ± 0.10	17.15 ± 0.03	⋯	18.47 ± 0.02	17.49 ± 0.02	16.77 ± 0.12
	WO1m	2012 May 1	⋯	17.79 ± 0.06	17.61 ± 0.07	⋯	⋯	18.52 ± 0.14	17.59 ± 0.07	16.69 ± 0.09
	WO1m	2013 Dec 15	19.46 ± 0.12	17.81 ± 0.03	17.61 ± 0.09	⋯	⋯	18.64 ± 0.10	17.54 ± 0.04	16.96 ± 0.10
	WO1m	2013 Dec 16	19.25 ± 0.06	17.80 ± 0.02	17.60 ± 0.04	⋯	20.07 ± 0.20	18.66 ± 0.06	17.53 ± 0.02	16.90 ± 0.03
	WO1m	2018 May 2	⋯	⋯	⋯	⋯	⋯	18.72 ± 0.16	17.60 ± 0.07	16.97 ± 0.08
	WOC28	2019 May 1	19.34 ± 0.06	⋯	⋯	⋯	⋯	⋯	17.54 ± 0.04	⋯
	WOC28	2019 May 4	19.40 ± 0.04	⋯	⋯	⋯	⋯	⋯	17.57 ± 0.02	⋯
	WOC28	2019 May 5	19.38 ± 0.05	⋯	⋯	⋯	⋯	⋯	17.57 ± 0.03	⋯
	LCO-1m	2020 Mar 27	19.59 ± 0.02	17.86 ± 0.01	17.63 ± 0.01	17.34 ± 0.01	⋯	⋯	⋯	⋯

Notes.
[a] Unless otherwise noted, observations made after 2014 with the WO1m utilized the SBIG STX16803 camera rather than the PI VA1300B camera. See Section 3.5 for details on the detectors.
[b] Used the PI VA1300B camera.

Thomas et al.

Table 12
Rest-frame UV Flux Densities and α_{ox} Data for the Chandra Sources

Quasar	JD	F_λ[a]	Obs.	Band	α_{ox}[b]	Δt[c]
Q0000−263	2,455,809.5	2.41 ± 0.04	WO1m	R	−1.70 ± 0.03	1.4
	2,456,185.5	2.35 ± 0.07	WO1m	R	−1.77 ± 0.04	2.4
	2,456,186.5	2.39 ± 0.03	WO1m	R	⋯	⋯
	2,456,541.5	2.29 ± 0.05	WOC18	R	−1.78 ± 0.04	0.2
	2,456,920.5	2.62 ± 0.08	WOC18	R	−1.75 ± 0.04	0.7
	2,456,921.5	2.57 ± 0.05	WOC18	R	⋯	⋯
	2,456,927.7	1.49 ± 0.19	LCO-dP	V	⋯	⋯
	2,458,709.5	2.86 ± 0.11	WOC28	R	−1.86 ± 0.05	0.2
	2,459,038.6	2.78 ± 0.05	LCO-1m	r'	−1.71 ± 0.04	1.4
BR 0351−1034	2,455,624.2	0.33 ± 0.02	WO1m	R	⋯	⋯
	2,455,626.2	0.37 ± 0.01	WO1m	r'	⋯	⋯
	2,455,831.5	0.31 ± 0.01	WO1m	R	−1.65 ± 0.07	0.7
	2,455,864.8	0.30 ± 0.01	LCO-dP	R	−1.75 ± 0.08	0.4
	2,456,509.8	0.15 ± 0.01	LCO-dP	V	⋯	⋯
	2,456,523.5	0.33 ± 0.03	WO1m	R	−1.50 ± 0.06	6.0
	2,456,987.5	0.36 ± 0.02	WO1m	R	⋯	⋯
	2,456,988.5	0.37 ± 0.01	LCO-dP	R	−1.76 ± 0.06	0.2
	2,458,790.5	0.52 ± 0.06	WOC18	r'	⋯	⋯
	2,458,791.5	0.40 ± 0.04	WOC18	r'	−1.67 ± 0.06	< 0.1
	2,458,806.4	0.36 ± 0.03	WOC28	r'	⋯	⋯
	2,459,160.8	0.43 ± 0.12	LCO-1m	r'	−1.60 ± 0.08	1.8
PSS 0926+3055	2,455,625.2	2.81 ± 0.06	WO1m	I	−1.76 ± 0.04	0.3
	2,455,962.3	2.68 ± 0.11	WO1m	I	−1.75 ± 0.05	4.4
	2,456,428.5	2.87 ± 0.03	WO1m	I	−1.75 ± 0.04	0.8
	2,456,681.5	3.36 ± 0.07	WO1m	I	−1.73 ± 0.04	1.2
	2,458,187.4	2.50 ± 0.02	WO1m	I	−1.90 ± 0.06	0.3
	2,458,189.3	2.59 ± 0.14	WOC18	I	⋯	⋯
	2,458,494.4	2.96 ± 0.08	WOC28	i'	−1.63 ± 0.04	0.6
	2,458,882.8	2.91 ± 0.03	LCO-1m	i'	−1.84 ± 0.05	1.8
PSS 1326+0743	2,455,629.6	1.76 ± 0.04	WO1m	R	−1.71 ± 0.04	0.4
	2,455,635.5	1.74 ± 0.03	WO1m	R	⋯	⋯
	2,456,049.3	1.59 ± 0.11	WO1m	R	−1.65 ± 0.04	0.3
	2,456,642.5	1.65 ± 0.06	WO1m	R	−1.56 ± 0.05	1.9
	2,458,241.3	1.57 ± 0.10	WO1m	R	−1.70 ± 0.05	0.5
	2,458,605.4	1.66 ± 0.61	WOC28	R	−1.64 ± 0.04	0.4
	2,458,608.4	1.16 ± 0.02	WOC28	R	⋯	⋯
	2,458,609.3	1.16 ± 0.03	WOC28	R	⋯	⋯
	2,458,936.2	1.70 ± 0.02	LCO-1m	i'	−1.64 ± 0.06	0.3

Note. For each source, α_{ox} is given only for the shortest time separations between the optical and Chandra observations.
[a] Flux density at rest-frame 1450 Å in units of 10^{-16} erg cm^{-2} s^{-1} Å^{-1}, extrapolated from the flux density at the effective wavelength of the respective band, assuming a continuum of the form $f_\lambda \propto \lambda^{-1.5}$ (corresponding to $f_\nu \propto \nu^{-0.5}$; Vanden Berk et al. 2001).
[b] Errors at the 1σ level on α_{ox} were derived according to Section 1.7.3 of Lyons (1991), given the errors on the rest-frame UV flux densities and the errors on the X-ray fluxes from Table 3.
[c] Rest-frame days between the ground-based and Chandra observations.

6. All four sources showed epoch-to-epoch variations in α_{ox} on the order of $\langle\Delta\alpha_{ox}\rangle \sim 0.09 \pm 0.01$; however, only PSS 0926+3055 is formally considered variable in α_{ox} over its entire light curve. Variations in α_{ox} are contemporaneous with the X-ray variability, supporting the suggestion that X-ray variability dominates the scatter in the optical-to-X-ray spectral slope. Overall, α_{ox} variations are consistent with those of RQQs at lower redshifts.

We aim at continuing this monitoring project in order to (1) extend the temporal baseline, (2) provide the longest-term and most thorough X-ray time-series analysis, and (3) explore short-term behavior, i.e., hourly to daily timescales in the rest frame of RQQs at $z \sim 4$; we will also increase the

exposure times in future observations given the loss of sensitivity of the ACIS detector (see Appendix A). The Chandra monitoring project will be complementary to the eROSITA survey (Predehl 2014), which has the capability to detect sources at $z > 4$ but may not provide light curves with sufficiently high S/Ns for meaningful time-series analyses of such sources.
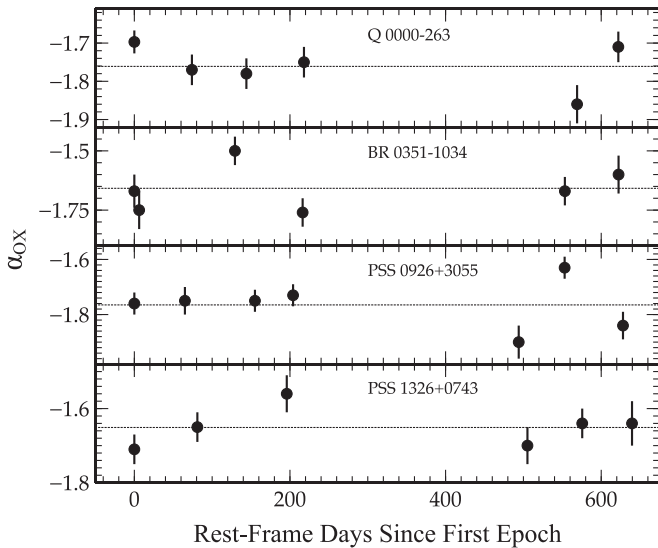
Figure 7. Optical-to-X-ray spectral slope, α_{ox}, plotted as a function of rest-frame days since the first optical epoch. The dashed line in each panel is the mean α_{ox} for the object over all epochs. The large α_{ox} dispersion in the later epochs of PSS 0926+3055 correspond to significant epoch-to-epoch soft-band X-ray variability, suggesting that scatter in α_{ox} is dominated by X-ray variability.
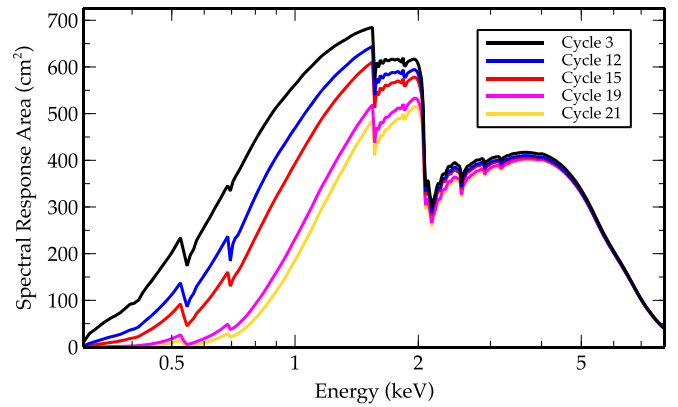

Figure A1. Effective response area of the ACIS-S detector is plotted against energy over select observations of PSS 0926+3055 in our monitoring program. The detector is continually losing effective area at all energy levels (loss at energies >5 keV can be seen in Figure A2). Detector response below 2 keV is degrading faster than higher energies and is now nearly zero below 0.5 keV.

Appendix A
Reduced Sensitivity in the ACIS Soft Band

Townsley et al. (2000) reported on damage to the ACIS by a bombardment of charged particles in Earth's radiation belts, resulting in increased CTI and causing QE to vary with photon energy and the position on the detector. Alongside this CTI is an additional effect of contamination buildup on the CCDs,[22] which the CXC reports to have markedly increased in 2009.[23] The rapid increase in contaminant has reduced QE even further and limited response to ultrasoft- and soft-band photon energies.

All data reduction using CIAO accounts for the CTI with CALDB, which is updated regularly throughout the Chandra cycles (i.e., years), but there is still a loss of information with the instrument being less sensitive to softer photons. The detector's spectral response areas (i.e., "effective" area accounting for QE) for select observations of PSS 0926 +3055 in the monitoring program are presented in Figure A1.

It can be seen that detector response is affected at all energies and is reduced considerably below $\sim$2 keV. In Figure A2, the same detector response areas are normalized to that of the first cycle in our monitoring program. The response in the ultrasoft band is now less than 5% of that in Cycle 3, and the response in the soft band ranges from 5% at 0.5 keV to 80% at 2 keV of that in Cycle 3.

Effects of this loss of sensitivity can be seen in Figure 1, which is composed of fluxes given in Table 3. For each object, the exact same instrument, CCDs, and exposure times were used across all epochs (with the exception of the two $\sim$6 ks Cycle 3 observations, which used an additional CCD on the detector). There is a noticeable increase in the size of the error bars for the soft-band flux (left) from Cycle 3 in 2003 to Cycle 21 in 2019–2020, whereas the error bars for the hard-band flux remain relatively consistent. Papers I and II reported counts in the ultrasoft band for each object and epoch, but in recent cycles, the ultrasoft sensitivity is effectively reduced to zero. An upper limit of three counts in the ultrasoft band was recorded for each object in Cycles 19–21, while there were detected counts in the majority of all previously reported epochs.

To illustrate the practical difference in calibration and soft-photon response, we used Chandra PIMMS to estimate the flux of a Cycle 3 observation with a soft-band count rate of 7.5×10^{-3} photons s^{-1}. We then used the same count rate to predict the flux in Cycle 21, our latest observation Cycle. The Cycle 21 flux estimate returned was three times that of Cycle 3, given the same count rate and model parameters.

Appendix B
Reprocessed Epochs from Papers I and II

The previous Chandra observations reported in Papers I and II utilized Chandra PIMMS to estimate source fluxes, effective photon indices (Γ_{eff}), and rest-frame 2 keV Galactic-absorption-corrected flux densities. This tool is intended for observation *planning* and should not be used on observed data owing to outdated instrument calibration predictions. Given the QE issues detailed above, the potential effect on the calibration of flux in a time-series analysis over the lifetime of the instrument is not negligible. See Section 2 for further details.

To obviate consideration of the potential offsets, we opted to calculate source fluxes by spectral modeling of the individual
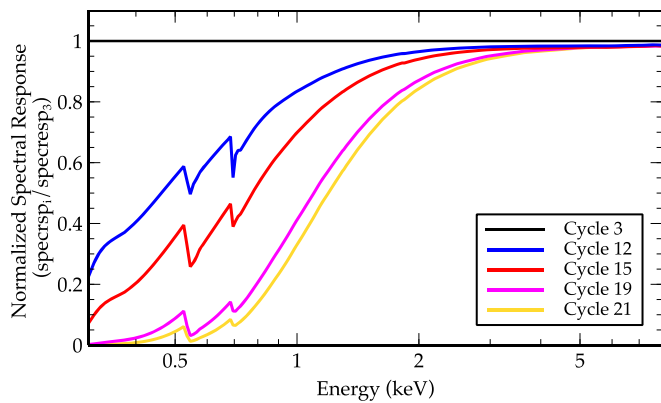
Figure A2. Effective response area, normalized to the first cycle in our monitoring program, of the ACIS-S detector is plotted against energy over select observations of PSS 0926+3055 in our monitoring program. At all energies, detector response is reduced, and at energies $\lesssim 0.5$ keV, detector response is less than 5% of that in Cycle 3.

Table B1
Spectral X-Ray Measurements

Object	Cycle	$\Gamma_{\rm eff}$ [a]	$f_{2\,\rm keV}$ [a]
Q0000−263	12	2.1 ± 0.4	2.18
	13	1.8 ± 0.4	1.38
	14	$1.9^{+0.6}_{-0.5}$	1.30
	15	$1.9^{+0.5}_{-0.4}$	1.70
BR 0351−1034	12	1.8 ± 1.0	0.37
	13	$1.5^{+0.9}_{-0.8}$	0.21
	14	$2.1^{+0.7}_{-0.6}$	1.05
	15	$1.1_{\pm 0.8}$	0.26
PSS 0926+3055	3	1.7 ± 0.4	1.90
	12	$1.7^{+0.5}_{-0.4}$	1.78
	13	2.0 ± 0.6	1.86
	14	1.6 ± 0.4	1.95
	15	1.8 ± 0.5	2.60
PSS 1326+0734	3	1.7 ± 0.4	1.62
	12	1.6 ± 0.5	1.52
	13	1.7 ± 0.5	1.93
	14	2.4 ± 0.6	3.44
	15	$2.1^{+0.5}_{-0.4}$	2.21

Note.
[a] Effective photon indices (0.5–8.0 keV; 90% confidence) were estimated by spectral modeling in Sherpa. See Section 2 for details on the assumed model. Galactic-absorption-corrected flux density at rest-frame 2 keV in units of 10^{-31} erg cm^{-2} s^{-1} Hz^{-1} was estimated with the PIMMS command-line tool v4.11b (Mukai 1993) by extrapolating the respective soft-band flux (see Table 3) and $\Gamma_{\rm eff}$.

observations using XSPEC models in Sherpa v14.3. Each observation was fit over 0.5–8.0 keV with a single power-law model convolved with a photoelectric absorption model (xsphabs*xspowerlaw) using the *cstat* statistic on data grouped to a minimum of one count per energy bin. Then, the models were frozen and convolved with the xscflux model to calculate energy flux. Using the soft-band flux and $\Gamma_{\rm eff}$, we used the PIMMS command-line tool to estimate the rest-frame 2 keV flux density. The effective photon index and flux density for each observation reported in Papers I and II are reported in Table B1.

ORCID iDs

Marcus O. Thomas (ORCID) https://orcid.org/0000-0002-2456-3209
Ohad Shemmer (ORCID) https://orcid.org/0000-0003-4327-1460
W. N. Brandt (ORCID) https://orcid.org/0000-0002-0167-2453
Maurizio Paolillo (ORCID) https://orcid.org/0000-0003-4210-7693
Shai Kaspi (ORCID) https://orcid.org/0000-0002-9925-534X
Cristian Vignali (ORCID) https://orcid.org/0000-0002-8853-9611
Paulina Lira (ORCID) https://orcid.org/0000-0003-1523-9164
Donald P. Schneider (ORCID) https://orcid.org/0000-0001-7240-7449

References

Allevato, V., Paolillo, M., Papadakis, I., & Pinto, C. 2013, ApJ, 771, 9
Almaini, O., Lawrence, A., Shanks, T., et al. 2000, MNRAS, 315, 325
Arnaud, K. A. 1996, in ASP Conf. Ser. 101, Astronomical Data Analysis Software and Systems V, ed. G. H. Jacoby & J. Barnes (San Francisco, CA: ASP), 17
Aschenbach, B., Bräuninger, H., Briel, U., et al. 1981, SSRv, 30, 569
Bechtold, J., Elvis, M., Fiore, F., et al. 1994, AJ, 108, 374
Bessell, M. S., Castelli, F., & Plez, B. 1998, A&A, 333, 231
Blanton, M. R., Bershady, M. A., Abolfathi, B., et al. 2017, AJ, 154, 28
Cash, W. 1979, ApJ, 228, 939
Chen, C. T. J., Brandt, W. N., Luo, B., et al. 2018, MNRAS, 478, 2132
Chiaraluce, E., Vagnetti, F., Tombesi, F., & Paolillo, M. 2018, A&A, 619, A95
Dickey, J. M., & Lockman, F. J. 1990, ARA&A, 28, 215
Ferrero, E., & Brinkmann, W. 2003, A&A, 402, 465
Fiore, F., Laor, A., Elvis, M., Nicastro, F., & Giallongo, E. 1998, ApJ, 503, 607
Freeman, P., Doe, S., & Siemiginowska, A. 2001, Proc. SPIE, 4477, 76
Freeman, P. E., Kashyap, V., Rosner, R., & Lamb, D. Q. 2002, ApJS, 138, 185
Fukugita, M., Ichikawa, T., Gunn, J. E., et al. 1996, AJ, 111, 1748
Garmire, G. P., Bautz, M. W., Ford, P. G., Nousek, J. A., & Ricker, G. R. J. 2003, Proc. SPIE, 4851, 28
Gehrels, N. 1986, ApJ, 303, 336
Gehrels, N., Chincarini, G., Giommi, P., et al. 2004, ApJ, 611, 1005
Gibson, R. R., & Brandt, W. N. 2012, ApJ, 746, 54
Grupe, D., Mathur, S., Wilkes, B., & Elvis, M. 2004, AJ, 127, 1
Grupe, D., Mathur, S., Wilkes, B., & Osmer, P. 2006, AJ, 131, 55
Helfand, D. J., White, R. L., & Becker, R. H. 2015, ApJ, 801, 26
Jansen, F., Lumb, D., Altieri, B., et al. 2001, A&A, 365, L1
Just, D. W., Brandt, W. N., Shemmer, O., et al. 2007, ApJ, 665, 1004
Kaastra, J. S. 2017, A&A, 605, A51
Kaspi, S., Brandt, W. N., Maoz, D., et al. 2007, ApJ, 659, 997
Kaspi, S., Brandt, W. N., & Schneider, D. P. 2000, AJ, 119, 2031
Kellermann, K. I., Sramek, R., Schmidt, M., Shaffer, D. B., & Green, R. 1989, AJ, 98, 1195
Kelly, B. C., Treu, T., Malkan, M., Pancoast, A., & Woo, J.-H. 2013, ApJ, 779, 187
La Franca, F., Bianchi, S., Ponti, G., Branchini, E., & Matt, G. 2014, ApJL, 787, L12
Lanzuisi, G., Ponti, G., Salvato, M., et al. 2014, ApJ, 781, 105
Lawrence, A., & Papadakis, I. 1993, ApJL, 414, L85
Luo, B., Brandt, W. N., Xue, Y. Q., et al. 2017, ApJS, 228, 2
Lusso, E., & Risaliti, G. 2016, ApJ, 819, 154
Lyons, L. 1991, A Practical Guide to Data Analysis for Physical Science Students (Cambridge: Cambridge Univ. Press)
MacLeod, C. L., Ivezić, Ž., Sesar, B., et al. 2012, ApJ, 753, 106
Manners, J., Almaini, O., & Lawrence, A. 2002, MNRAS, 330, 390
McHardy, I. M., Koerding, E., Knigge, C., Uttley, P., & Fender, R. P. 2006, Natur, 444, 730
Mighell, K. J. 1999, ApJ, 518, 380
Mukai, K. 1993, Legacy, 3, 21
Mushotzky, R. F., Done, C., & Pounds, K. A. 1993, ARA&A, 31, 717
Nanni, R., Gilli, R., Vignali, C., et al. 2018, A&A, 614, A121
Nanni, R., Vignali, C., Gilli, R., Moretti, A., & Brandt, W. N. 2017, A&A, 603, A128
Navas-Palencia, G. 2020, arXiv:2001.08025
Nousek, J. A., & Shue, D. R. 1989, ApJ, 342, 1207
Paolillo, M., Papadakis, I., Brandt, W. N., et al. 2017, MNRAS, 471, 4398
Paolillo, M., Schreier, E. J., Giacconi, R., Koekemoer, A. M., & Grogin, N. A. 2004, ApJ, 611, 93

Papadakis, I. E., Chatzopoulos, E., Athanasiadis, D., Markowitz, A., & Georgantopoulos, I. 2008, A&A, 487, 475

Park, T., Kashyap, V. L., Siemiginowska, A., et al. 2006, ApJ, 652, 610

Piconcelli, E., Jimenez-Bailón, E., Guainazzi, M., et al. 2005, A&A, 432, 15

Predehl, P. 2014, AN, 335, 517

Ricci, C., Kara, E., Loewenstein, M., et al. 2020, ApJL, 898, L1

Richards, G. T., Strauss, M. A., Fan, X., et al. 2006, AJ, 131, 2766

Shemmer, O., Brandt, W. N., Netzer, H., Maiolino, R., & Kaspi, S. 2006a, ApJL, 646, L29

Shemmer, O., Brandt, W. N., Paolillo, M., et al. 2014, ApJ, 783, 116

Shemmer, O., Brandt, W. N., Paolillo, M., et al. 2017, ApJ, 848, 46

Shemmer, O., Brandt, W. N., Schneider, D. P., et al. 2006b, ApJ, 644, 86

Shemmer, O., Brandt, W. N., Vignali, C., et al. 2005, ApJ, 630, 729

Spergel, D. N., Bean, R., Doré, O., et al. 2007, ApJS, 170, 377

Steffen, A. T., Strateva, I., Brandt, W. N., et al. 2006, AJ, 131, 2826

Timlin, J. D. I., Brandt, W. N., Zhu, S., et al. 2020, MNRAS, 498, 4033

Townsley, L. K., Broos, P. S., Garmire, G. P., & Nousek, J. A. 2000, ApJL, 534, L139

Trevese, D., Boutsia, K., Vagnetti, F., Cappellaro, E., & Puccetti, S. 2008, A&A, 488, 73

Turner, T. J., George, I. M., Nandra, K., & Turcan, D. 1999, ApJ, 524, 667

Vagnetti, F., Middei, R., Antonucci, M., Paolillo, M., & Serafinelli, R. 2016, A&A, 593, A55

Vagnetti, F., Turriziani, S., & Trevese, D. 2011, A&A, 536, A84

Vanden Berk, D. E., Richards, G. T., Bauer, A., et al. 2001, AJ, 122, 549

Vaughan, S., Edelson, R., Warwick, R. S., & Uttley, P. 2003, MNRAS, 345, 1271

Vignali, C., Brandt, W. N., Fan, X., et al. 2001, AJ, 122, 2143

Vignali, C., Brandt, W. N., Schneider, D. P., Garmire, G. P., & Kaspi, S. 2003, AJ, 125, 418

Vignali, C., Brandt, W. N., Schneider, D. P., & Kaspi, S. 2005, AJ, 129, 2519

Vito, F., Brandt, W. N., Bauer, F. E., et al. 2019, A&A, 630, A118

Wang, F., Fan, X., Yang, J., et al. 2021, ApJ, 908, 53

Wang, S., Liu, J., Qiu, Y., et al. 2016, ApJS, 224, 40

Weisskopf, M. C., Tananbaum, H. D., Van Speybroeck, L. P., & O'Dell, S. L. 2000, Proc. SPIE, 4012, 2

Yang, G., Brandt, W. N., Luo, B., et al. 2016, ApJ, 831, 145